Non-equilibrium effects of diatomic and polyatomic gases on the shock-vortex interaction based on the second-order constitutive model of the Boltzmann-Curtiss equation

S. Singh, A. Karchani, R. S. Myong*

School of Mechanical and Aerospace Engineering and ACTRC & ReCAPT, Gyeongsang National University, Jinju, Gyeongnam 52828, South Korea

Abstract: The rotational mode of molecules plays a critical role in the behaviour of diatomic and polyatomic gases away from equilibrium. In order to investigate the essence of the non-equilibrium effects, the shock-vortex interaction (SVI) problem was investigated by employing an explicit modal discontinuous Galerkin method. In particular, the first- and second-order constitutive models for diatomic and polyatomic gases derived rigorously from the Boltzmann-Curtiss kinetic equation were solved in conjunction with the physical conservation laws. As compared with a monatomic gas, the non-equilibrium effects result in a substantial change in flow fields in both macroscale and microscale shock-vortex interactions. Specifically, the computational results showed three major effects of diatomic and polyatomic gases on the shock-vortex interaction; (i) the generation of third sound waves and additional reflected shock waves with strong and enlarged expansion, (ii) the dominance of viscous vorticity generation, (iii) an increase in enstrophy with increasing bulk viscosity, related to the rotational mode of gas molecules. Moreover, it was shown that there is a significant discrepancy in flow fields between the microscale and macroscale shock-vortex interactions in diatomic and polyatomic gases. The quadrupolar acoustic wave source structures, which are typically observed in macroscale shock-vortex interactions, were not found in any microscale shock-vortex interactions. The physics of the shock-vortex interaction was also investigated in detail to examine vortex deformation and evolution dynamics over an incident shock wave. A comparative study of first- and second-order constitutive models was also conducted for enstrophy and dissipation rate. Finally, the study was extended to the shock-vortex pair interaction (SVPI) case to examine the effects of pair interaction on vortex deformation and evolution dynamics.

* myong@gnu.ac.kr

I. INTRODUCTION

A gas particle can have various energy modes, including translational, rotational and vibrational modes. Translational mode is described by the random motion of gas particles. In addition to a translational mode, diatomic and polyatomic gas particles can also possess an internal mode, due to the rotation of atoms around an axis, as well as the vibration of atoms along an inter-nuclear axis. The internal modes of diatomic and polyatomic gases—the rotational and vibrational modes—are closely related to thermal non-equilibrium.

Among internal modes, the rotational mode is easily excited at room temperature, making it ubiquitous across whole flow conditions. In contrast, the vibrational mode becomes relevant only in gas flows where the temperature is greater than the vibrational excitation temperature; for example, 1000°K. For this reason, in the study of diatomic and polyatomic gases, the excitation of vibrational degrees of freedom is usually neglected.

The rotational non-equilibrium effect can be simply accounted for by introducing the excess normal stress associated with bulk viscosity. The so-called bulk viscosity has a long history, not only in compressible gas dynamics, but also in fluid dynamics in general. For example, the two-century old Navier-Stokes-Fourier equation (called NSF hereafter) is considered to be the *de facto* mathematical equation for every possible flow problem, including compressible gas dynamics. The NSF theory is built upon a critical assumption of the constitutive equations, introduced by Stokes[1] in 1845, that the bulk viscosity vanishes,

$$\mu_b \equiv \lambda + \frac{2}{3}\mu = 0, \text{ equivalently } \lambda = -\frac{2}{3}\mu. \tag{1}$$

Here μ_b, λ and μ represent the bulk viscosity, the second coefficient of viscosity and the shear viscosity of the fluid, respectively. The Stokes's hypothesis, mathematically expressed as (1), assumes that the dilatational term $(\nabla \cdot \mathbf{u})$ plays no role in the level of the constitutive equation of viscous stress, even though it may play a significant role in the level of conservation laws in general, like compressible gas flows.

Further, the origin of bulk viscosity is often attributed to pure phenomenological observation, such as interpreting it as the dissipation mechanism during a change in volume at a finite rate, rather than resorting to a fundamental microscopic kinetic theory.

While the Stokes's hypothesis is certainly legitimate in the case of monatomic gases like argon, there is ever increasing evidence that now indicates that this is not the case for non-monatomic gases[2-4]—like nitrogen (or air), methane, and carbon dioxide—that are far from local thermal equilibrium. Examples of such cases include the inner structure of strong shock waves, hypersonic entry into the Mars atmosphere, which consists mostly of carbon dioxide, the effects of bulk viscosity on the stability of the early universe, and the bulk viscosity of suspensions.[5-7]

It should also be noted that, from room temperature acoustic attenuation data, the bulk viscosity for carbon dioxide is known to be three orders of magnitude larger than its shear viscosity, indicating it has a highly dispersive nature which is dependent on frequency. In fact, in a recent experimental study[2] in 2016 on the role of dilatational (longitudinal acoustic) waves in a second-mode instability in the laminar-to-turbulence transition in hypersonic boundary layers, it was observed that, for a real diatomic gas, the growth and decay of the second mode is accompanied by a dilatation process which leads to about a 50% increase in dilatation dissipation, in comparison with the Stokes's hypothesis.

In a similar context, the interaction between shock waves and vortical flows has received considerable attention in gas dynamics and aeroacoustics. Studies include the enhancement of fuel-air mixing in combustion,[8] helicopter blades operating at supercritical speeds,[9] the shock noise generation in the design of advanced jet engines,[10] combustion instability,[11] and so on. In such flows, when a number of shock waves interact with vortices, the coupling between them dominates the flow field and produces a complicated flow pattern. Because of this complexity, a disturbance is generated which propagates along with the shock waves, resulting in a distortion phenomenon between the shock waves and vortices. The interaction alters or destroys the shock waves and the vortical flow structure.

The shock-vortex interaction (called SVI hereafter) has been the subject of extensive study, since it is one of the most simplified models of the interaction between shock waves and vortical flows. Over

the last few decades, significant efforts have been devoted to interpreting the physical phenomena of SVI through experiments, theoretical analysis, and numerical simulations.

Among these, Hollingsworth and Richards[12] carried out an early experiment and showed that SVI produces a cylindrical acoustic wave, consisting of alternating compression and rarefaction regions around the circumference. Later, the circumferential pressure distribution of the acoustic wave was measured by Dosanjh and Weeks.[13] A linear theory was proposed by Ribner[14] for describing the sound production mechanism and its quadrupolar nature in SVI. Ellzey *et al.*[15] investigated numerically SVI and found two acoustic waves with a quadrupolar nature. Subsequently, Inoue and Hattori[16] identified a third acoustic wave generated in planar SVI. Grasso and Pirozzoli[17] examined the interaction of a shock wave with a cylindrical vortex and investigated the dependence of shock distortion and vortex compression on the shock and vortex strength. Later, Zhang *et al*.[18] conducted a numerical study of a SVI with a strong vortex and found the multistage features of acoustic shock waves. Recently, multiple acoustic waves, quadrupolar in nature and successively out of phase, were captured in a numerical simulation of SVI by Chatterjee and Vijayraj.[19]

In addition, studies of the shock-vortex pair interaction (called SVPI hereafter) have been carried out to better understand the nature of more complicated shock flow interactions. However, the study of SVPI has been very limited compared to SVI, due to the complexity associated with the physics of the SVPI problem, including shock wave distortion, shock focusing and the different mechanisms of sound generation.[16, 20-22]

Interestingly, most of the earlier theoretical and computational studies have investigated the SVI and SVPI problems at the macroscale (macro hereafter) where the thermal non-equilibrium effects are assumed to be negligible. Basically, these studies are based on compressible Euler or NSF equations, which are derived from the Boltzmann kinetic equation with the assumption of thermal-equilibrium and near thermal-equilibrium, respectively. Moreover, virtually all the previous studies are based on the Stokes's hypothesis in which the rotational mode of diatomic and polyatomic gases is completely ignored in the level of constitutive equations of viscous stresses and heat flux.

There are a few studies available on microscale (micro hereafter) SVI in thermal non-equilibrium. Koffi *et al.*[23] conducted numerical simulations using the direct simulation Monte Carlo (DSMC)

method to characterize the mutual interactions of planar shocks with a micro-vortex. It was shown that, for the limited Mach and Knudsen numbers studied, the viscous attenuation of the vortex was found to dominate the gas flow in the micro SVI. Recently, Xiao and Myong carried out a numerical simulation of vorticity generation and vortex deformation in a micro SVI for a monatomic gas.[24] In their study, some unique characteristics were found in the micro SVI; for instance, the absence of a quadrupolar acoustic wave structure, which is a major feature of the macro SVI; an increase in the dissipation rate during the strong interaction; and a decrease in enstrophy during the weak interaction.

At the microscale, the primary criterion used to measure the degree of non-equilibrium phenomena is the local Knudsen number, which is the ratio of mean free path to characteristic length. Previous studies have revealed that the classical description of NSF, or of Navier-Fourier (NF hereafter) without the Stokes's hypothesis based on first-order Boltzmann-based constitutive model, is only valid in flows near equilibrium, and is questionable in flows not-so-near equilibrium. As a consequence, simple modification of the NSF (or NF) theory using transport coefficients cannot solve the present bottleneck in the study of gas flows far from equilibrium.

In order to deal with this situation, a non-classical theory based on algebraic second-order Boltzmann–Curtiss-based constitutive relations for monatomic, diatomic, and polyatomic gases was developed by Myong.[25,26] Starting from the original Eu's generalized hydrodynamics,[27,28] the second-order constitutive models were developed from the viewpoint of the moment method applied to the Boltzmann-Curtiss kinetic equation[29] and the so-called balanced closure.[26] These second-order constitutive models for diatomic gases were validated by investigating compressive shock dominated gas flow[25] and velocity-shear dominated force-driven Poiseuille gas flow.[30]

In this study, encouraged by these developments, we aim to investigate the problem of the non-equilibrium effects of diatomic and polyatomic gases on SVI based on the second-order constitutive model of the Boltzmann-Curtiss kinetic equation. *To the best knowledge of the authors, no attempt has been made in the past to investigate the non-equilibrium effects of the rotational mode in diatomic and polyatomic gases* (*at micro as well as macro levels*) *on the SVI problem.* Further, the present study may be regarded as the first theoretical and computational attempt to investigate the strong interaction of two important non-equilibrium phenomena in diatomic and polyatomic

gases—compressive shock structure and velocity-shear of the vortex—using the fundamental microscopic Boltzmann-Curtiss kinetic theory and subsequent second-order constitutive equations, without resorting to pure phenomenological theory.

Toward this goal, we consider in depth the Boltzmann-Curtiss kinetic equation[25] for diatomic and polyatomic gases and derive the second-order constitutive equations for non-conserved variables as well as the conservation laws of conserved variables. The non-equilibrium effects of diatomic and polyatomic gases on the SVI problem are then studied systematically to highlight the differences, in comparison with the monatomic gas case. A comparative study of macro and micro SVI is also conducted to characterize the complicated flow fields. Additionally, the evolution dynamics of micro SVI are analysed for deeper understanding of the non-equilibrium effects of diatomic and polyatomic gases. Finally, the study is extended to the SVPI case in order to examine the effects of pair interaction on vortex deformation and evolution dynamics.

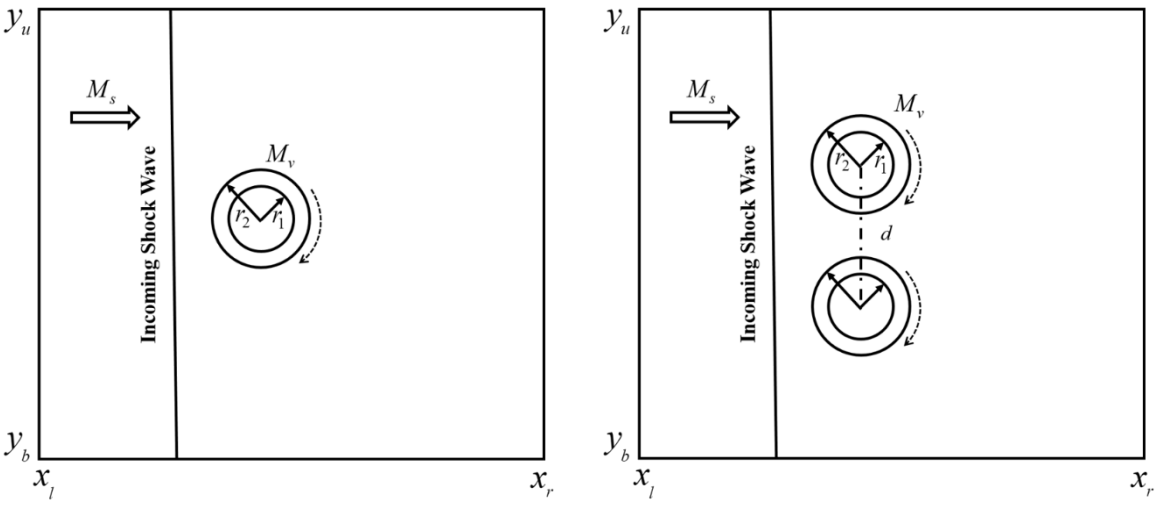

(a) Single vortex case (b) Vortex pair case

FIG.1. Schematic diagram of the flow model for single and vortex pair cases.

II. PROBLEM DEFINITION AND COMPUTATIONAL MODELS FOR THE SVI PROBLEM

A. Problem definition

A schematic diagram of the flow model used to simulate a shock wave interacting with a single vortex and a vortex pair is depicted in Fig. 1. The computational domain was designed to be rectangular $\left(x_l \le x \le x_r,\ y_b \le y \le y_u\right)$. Two computational domains with different sizes were used in the present work; one was a domain with a size of $x_r = -x_l = 0.0008\ \text{m}$, $y_u = -y_l = 0.0008\ \text{m}$ used for simulating the micro SVI cases; the other one was a domain with a size of $x_r = -x_l = 0.1\ \text{m}$, $y_u = -y_l = 0.1\ \text{m}$ used for simulating the macro SVI cases. Here, a moving shock wave and clockwise-rotating stationary vortices are considered. The shock wave moves from left to right with respect to the initial shock wave in the computational domain.

The location of the centre of the single vortex in the SVI was set to be (0, 0), while the location of the centre of the two vortices in the SVPI were set to be $\left(0, \pm d/2\right)$. The initial separation distance of the two vortices *d* was set to be 0.0002 m for the micro SVPI and 0.02 m for the macro SVPI.

A vortex was formed by selecting a composite vortex as the initial flow.[23,31] The composite vortex model consists of two regions; an inner core region and a surrounding region where the velocity gradually approaches zero. The rotational centre of the vortex is initially stationary, and the velocity distribution between the core radius r_1 and outer radius r_2 is determined before starting a simulation. In this flow, the maximum tangential velocity is found in the core radius while the tangential velocity outside the outer radius $\left(r > r_2\right)$ is set to zero. Inside the core $\left(r \le r_1\right)$, the velocity goes linearly to zero at $r = 0$. The size of the core radius r_1 has a significant effect on the flow field. Therefore, we considered a core radius from 8λ to 1000λ with a step of 2λ. From now on, the symbol $\lambda\,(= 6.26\times10^{-6}\ \text{m})$ represents the mean free path at the initial condition.

The tangential velocity distribution of a clockwise-rotating vortex is defined as follows,

$$u_\theta = \begin{cases} u_m \dfrac{r}{r_1}, & r \le r_1 \\ u_m \dfrac{r_1}{r_1^2 - r_2^2}\left(r - \dfrac{r_2^2}{r}\right), & r_1 \le r \le r_2 \\ 0, & r > r_2 \end{cases} \tag{2}$$

where u_θ is the azimuthal component of velocity, and u_m denotes the maximum tangential velocity. The temperature and the pressure in the quiescent field surrounding the vortex were also selected. Inside the vortex, the pressure, the density and the energy were determined by balancing the pressure gradients with the centripetal force which is equivalent to solving the following system,

$$\frac{dp}{dr} = \rho \frac{u_\theta^2}{r}, \ \frac{p}{\rho^\gamma} = K, \ p = \rho RT, \tag{3}$$

where γ is the specific heat ratio of gas, R is the gas constant, K is a constant, ρ is the density, p is the pressure, and T is the temperature. From the last two equations, it is straightforward to deduce that the pressure and density fields inside the vortex satisfy

$$p = p_1 \left(\frac{T}{T_1}\right)^{\frac{\gamma}{\gamma-1}}, \quad \rho = \rho_1 \left(\frac{T}{T_1}\right)^{\frac{1}{\gamma-1}}. \tag{4}$$

Using above equations, we can obtain the temperature from the following ordinary differential equation

$$\frac{dT}{dr} = \frac{\gamma - 1}{\gamma R} \frac{u_\theta^2}{r}. \tag{5}$$

This equation together with equation (4) allows us to compute the pressure and density distribution inside the vortex.

In general, the flow fields generated by interactions between the shock wave and vortices are largely affected by three flow parameters: the Mach numbers of the incoming shock wave and rotating vortex, M_s and M_v, respectively, as defined by the maximum tangential velocity of the vortex, and the core radius r_1. In this work, these flow parameters were chosen to demonstrate the effects of the shock wave, vortex strength and vortex size on the interaction. The Mach numbers of the incoming shock wave M_s were selected to range from 1.5 to 3.5 with a step of 0.5, while the Mach numbers of vortex M_v ranged from 0.6 (weak vortex) to 1.0 (strong vortex). The baseline case for our

computation was an incoming shock Mach number of $M_s = 2.0,$ a vortex Mach number of $M_v = 0.8,$ and a vortex core radius $r_1 = 10\lambda$ and 1000λ with $r_2 = 2r_1$. In the SVPI simulations, both of the vortices were assumed to have equal strength and the same clockwise-rotating direction.

B. The second-order constitutive model for diatomic and polyatomic gases

1. Boltzmann-Curtiss kinetic equation for diatomic and polyatomic gases and the exact conservation laws

The Boltzmann-Curtiss kinetic equation for diatomic (and linear polyatomic) molecules with a moment of inertia I_m and an angular momentum **j** can be expressed[29] as the following when there is no external field,

$$\left(\frac{\partial}{\partial t} + \mathbf{v}\cdot\nabla + \frac{j}{I_m}\frac{\partial}{\partial \psi}\right) f\left(\mathbf{v},\mathbf{r},\mathbf{j},\psi,t\right) = R[f], \tag{6}$$

where $f, \mathbf{v}, \mathbf{r}, \psi, j$ and $R[f]$ represent the distribution function, the particle velocity, the particle position, the azimuthal angle associated with the orientation of the particle, the magnitude of the angular momentum vector **j**, and the collision integral, respectively. When the angular momentum of the molecule related to the rotational mode is ignored, the Boltzmann-Curtiss kinetic equation recovers the original Boltzmann kinetic equation for a monatomic gas

$$\left(\frac{\partial}{\partial t} + \mathbf{v}\cdot\nabla\right) f\left(\mathbf{v},\mathbf{r},t\right) = C[f],$$

where $C[f]$ represents the Boltzmann collision integral of the interaction between two particles.

There are two different sets of macroscopic variables; the conserved variables $\left(\rho, \rho\mathbf{u}, \rho E\right)$ and the non-conserved variables $\left(\boldsymbol{\Pi}, \Delta, \mathbf{Q}\right),$ where **u** is the velocity vector, *E* is the total energy density, while $\boldsymbol{\Pi}$, Δ, **Q** represent the shear stress tensor, the excess normal stress, and the heat flux, respectively. These variables can be defined by a statistical formula

$$\phi^{(k)} = \left\langle h^{(k)} f \right\rangle, \tag{7}$$

where the angular bracket denotes the integration over the variables **v** and j. The $h^{(k)}$ indicates the molecular expressions for moments. The leading elements of the set of the conserved and non-conserved variables are defined as[27],

$$\begin{aligned} &\phi^{(1)} = \rho,\ \phi^{(2)} = \rho\mathbf{u},\ \phi^{(3)} = \rho E, \\ &\phi^{(4)} = \boldsymbol{\Pi} = \left[\mathbf{P}\right]^{(2)},\ \phi^{(5)} = \Delta = \frac{1}{3}\mathrm{Trace}\,\mathbf{P} - p,\ \phi^{(6)} = \mathbf{Q}, \end{aligned} \tag{8}$$

with the molecular expressions corresponding to this set

$$\begin{aligned} &h^{(1)} = m,\ h^{(2)} = m\mathbf{v},\ h^{(3)} = \frac{1}{2}mC^2 + H_{rot}, \\ &h^{(4)} = \left[m\mathbf{C}\mathbf{C}\right]^{(2)},\ h^{(5)} = \frac{1}{3}mC^2 - p/n,\ h^{(6)} = \left(\frac{1}{2}mC^2 + H_{rot} - m\hat{h}\right)\mathbf{C}, \end{aligned} \tag{9}$$

where m is the molecular mass, $\mathbf{C} = \mathbf{v} - \mathbf{u}$ is the peculiar velocity of the molecule, n is the number density per unit mass, $\hat{h}$ is the enthalpy density per unit mass, and $H_{rot} = j^2/2I_m$ is the rotational Hamiltonian of the particle. The viscous stresses $\boldsymbol{\Pi}$ and Δ are related to the stress tensor **P** through the relation

$$\mathbf{P} = \left(p + \Delta\right)\mathbf{I} + \boldsymbol{\Pi}. \tag{10}$$

Here, **I** is the unit second rank tensor, $p = nk_BT = \rho RT$ is the equation of state. The symbol T denotes the overall temperature related to both translational and rotational energy. The symbol $\left[\mathbf{A}\right]^{(2)}$ denotes the traceless symmetric part of the second-rank tensor **A**,

$$\left[\mathbf{A}\right]^{(2)} = \frac{1}{2}\left(\mathbf{A} + \mathbf{A}^t\right) - \frac{1}{3}\mathbf{I}\,\mathrm{Trace}\,\mathbf{A}. \tag{11}$$

The conservation laws of mass, momentum, and total energy for diatomic and polyatomic gases can be derived directly from the Boltzmann-Curtiss kinetic equation by noting that the molecular expressions for conserved variables (9) are collision invariants and thus there is no dissipation term, i.e. $\left\langle \phi^{(1,2,3)} R[f] \right\rangle = 0$. After differentiating the statistical definition of the conserved variables with time and combining them with the Boltzmann-Curtiss equation, the following conservation laws, all of which are an *exact* consequence of the Boltzmann-Curtiss kinetic equation, can be derived,[25, 27]

$$\frac{\partial}{\partial t}\begin{bmatrix}\rho\\ \rho\mathbf{u}\\ \rho E\end{bmatrix}+\nabla\cdot\begin{bmatrix}\rho\mathbf{u}\\ \rho\mathbf{u}\mathbf{u}+p\mathbf{I}\\ (\rho E+p)\mathbf{u}\end{bmatrix}+\nabla\cdot\begin{bmatrix}0\\ \Pi+\Delta\mathbf{I}\\ (\Pi+\Delta\mathbf{I})\mathbf{u}+\mathbf{Q}\end{bmatrix}=0. \tag{12}$$

In this expression (12), the symbol *E* denotes the total energy which can be defined as,

$$E=\frac{1}{2}\mathbf{u}\cdot\mathbf{u}+\frac{1}{(\gamma-1)}\frac{p}{\rho}. \tag{13}$$

After the following dimensionless variables and parameters are introduced,

$$\begin{aligned}&t^*=\frac{t}{(L/u_r)},\ \boldsymbol{x}^*=\frac{\boldsymbol{x}}{L},\ \mu^*=\frac{\mu}{\mu_r},\ k^*=\frac{k}{k_r},\ \boldsymbol{u}^*=\frac{\boldsymbol{u}}{u_r},\ p^*=\frac{p}{p_r},\ \rho^*=\frac{\rho}{\rho_r},\\ &T^*=\frac{T}{T_r},\ C_p^*=\frac{C_p}{C_{pr}},\ E^*=\frac{E}{u_r^2},\ \boldsymbol{\Pi}^*=\frac{\boldsymbol{\Pi}}{(\mu_r u_r/L)},\ \Delta^*=\frac{\Delta}{(\mu_{b_r}u_r/L)},\ \mathbf{Q}=\frac{\mathbf{Q}}{(k_r\Delta T/L)},\end{aligned} \tag{14}$$

where the subscript *r* stands for the reference state, *L* denotes the characteristic length, c_p denotes the heat capacity per mass at constant pressure, μ, μ_b, k are the Chapman-Enskog shear viscosity, the bulk viscosity, and the thermal conductivity, respectively, the non-dimensional conservation laws for diatomic and polyatomic gases (with the asterisks omitted for notational brevity) can be written as,[25]

$$\frac{\partial}{\partial t}\begin{bmatrix}\rho\\ \rho\mathbf{u}\\ \rho E\end{bmatrix}+\nabla\cdot\begin{bmatrix}\rho\mathbf{u}\\ \rho\mathbf{u}\mathbf{u}+\frac{1}{\gamma M^2}p\mathbf{I}\\ \left(\rho E+\frac{1}{\gamma M^2}p\right)\mathbf{u}\end{bmatrix}+\nabla\cdot\frac{1}{\mathrm{Re}}\begin{bmatrix}0\\ \boldsymbol{\Pi}+\Delta\mathbf{I}\\ (\boldsymbol{\Pi}+\Delta\mathbf{I})\cdot\mathbf{u}+\frac{1}{Ec\,\mathrm{Pr}}\mathbf{Q}\end{bmatrix}=0. \tag{15}$$

Here, the dimensionless parameters such as Mach number (*M*), Reynolds number (Re), Eckert number (*Ec*) and Prandtl number (Pr) can be defined as

$$M\equiv\frac{u_r}{\sqrt{\gamma RT_r}},\ \mathrm{Re}\equiv\frac{\rho_r u_r L}{\mu_r},\ Ec\equiv(\gamma-1)M^2,\ \mathrm{Pr}\equiv\frac{c_{p_r}\mu_r}{k_r}. \tag{16}$$

The specific heat ratio γ is assumed to be 5/3 for argon gas, 7/5 for nitrogen gas, and 1.289 for methane gas. The value of the Prandtl number (Pr) may be calculated through Eucken's relation

$$\mathrm{Pr}=\frac{4\gamma}{9\gamma-5}. \tag{17}$$

In the present work, the speed of sound before the shock wave was chosen to be the reference velocity u_r, resulting in $M = 1$. Nonetheless, the reference Mach number M is retained in the non-dimensional equations to show its role in the formulation. In addition, the core radius of the vortex r_1 was used as the reference length L.

2. First-order Boltzmann-Curtiss-based (Navier-Fourier) constitutive model

After differentiating the statistical definition of the non-conserved variables $\phi^{(4,5,6)} = \left\langle h^{(4,5,6)} f \right\rangle$ with time and combining them with the Boltzmann-Curtiss equation, the following first-order Boltzmann-Curtiss-based constitutive model of the shear stress tensor, the excess normal stress, and the heat flux vector can be obtained;

$$\mathbf{\Pi} = -2\mu\left[\nabla\mathbf{u}\right]^{(2)}, \quad \Delta = -\mu_b \nabla\cdot\mathbf{u}, \quad \mathbf{Q} = -k\nabla T. \tag{18}$$

Once the Stokes's hypothesis (1) is applied, that is, $\mu_b = 0$, the first-order NF constitutive equations (18) are reduced to the well-known linear NSF constitutive equations. It should be noted that these first-order linear relations were obtained after very crude approximations; all kinematic terms except for the thermodynamic force term were neglected in the moment equations and the collision-related dissipation terms $\left\langle \phi^{(4,5,6)} R[f] \right\rangle$ were linearized. In these expressions, the following Chapman-Enskog linear transport coefficients can be employed

$$\mu = T^s, \mu_b = f_b \mu, k = T^s, \tag{19}$$

where s stands for the index of the inverse power laws of gas molecules, given as

$$s = \frac{1}{2} + \frac{2}{(\nu - 1)}. \tag{20}$$

Here the parameter ν is the exponent of the inverse power laws for the gas particle interaction potentials. The value of s was assumed to be 0.81 for argon gas, 0.78 for nitrogen, and 0.84 for methane gas.[32] The factor $f_b = \mu_b / \mu$ is the ratio of the bulk viscosity to the shear viscosity. Its value can be determined using a sound wave absorption measurement. The f_b values for argon, nitrogen and methane gases were considered to be 0.0, 0.8 and 1.33, respectively, based on experiments.[33]

3. Second-order Boltzmann-Curtiss-based constitutive model

Similarly, the second-order constitutive model can be derived by first differentiating the statistical definition of the non-conserved variables $\phi^{(4,5,6)}$ with time and then combining them with the Boltzmann-Curtiss kinetic equation. However, it turned out that the derivation of the second-order constitutive model is extremely difficult, mainly due to two fundamental issues; the so-called closure problem and accurate treatment of the dissipation terms $\left\langle \phi^{(4,5,6)} R[f] \right\rangle$, both of which have remained unsolved for several decades.

In order to accurately calculate the dissipation terms while making the underline theory compatible with the second law of thermodynamics, Eu in 1980 proposed a canonical distribution function in the exponential form, instead of the usual polynomial form, after recognizing the logarithmic form of the non-equilibrium entropy production.[28] On the other hand, Myong in 2014 proposed a new closure theory from a keen observation of the fact that, when closing open terms in the moment equations derived from the kinetic equation, the number of places to be closed was two (movement and interaction), rather than one (movement only), having been misled by the Maxwellian molecule assumption in the previous theory.[26] Therefore, the order of approximations in handling the two terms—kinematic (movement) and dissipation (interaction) terms—must be the same; for instance, second-order for both terms.

Once these tenets—the Eu's cumulant expansion based on the canonical distribution function in the exponential form to the explicit calculation of the dissipation term, and the aforementioned new balanced closure—are applied to the moment equations and after the second-order approximation, the following second-order constitutive model can be derived from the Boltzmann-Curtiss kinetic equation[25,28]

$$
\begin{aligned}
\hat{\boldsymbol{\Pi}} q_{2nd}(c\hat{R}) &= \left(1+ f_b\hat{\Delta}\right)\hat{\boldsymbol{\Pi}}_0 + \left[\hat{\boldsymbol{\Pi}}\cdot\nabla\hat{\mathbf{u}}\right]^{(2)}, \\
\hat{\Delta} q_{2nd}(c\hat{R}) &= \hat{\Delta}_0 + \frac{3}{2} f_b \left(\hat{\boldsymbol{\Pi}} + f_b\hat{\Delta}\mathbf{I}\right) : \nabla\hat{\mathbf{u}}, \\
\hat{\mathbf{Q}} q_{2nd}(c\hat{R}) &= \left(1+ f_b\hat{\Delta}\right)\hat{\mathbf{Q}}_0 + \hat{\boldsymbol{\Pi}}\cdot\hat{\mathbf{Q}}_0 .
\end{aligned}
\tag{21}
$$

Here the caret (^) over a symbol represents a quantity with the dimension of the ratio of the stress to the pressure. Note that the relationships in the second-order Boltzmann-Curtiss-based constitutive model are nonlinear and a coupled function of the velocity and temperature gradients. The values of $\boldsymbol{\Pi}_0$, Δ_0, and $\mathbf{Q}_0$ are determined by the Newtonian law of shear and bulk viscosity, and the Fourier law of heat conduction, respectively,

$$\boldsymbol{\Pi}_0 = -2\mu\left[\nabla\mathbf{u}\right]^{(2)}, \quad \Delta_0 = -\mu_b \nabla\cdot\mathbf{u}, \quad \mathbf{Q}_0 = -k\nabla T. \tag{22}$$

All terms in equations (21) are normalized by introducing proper variables and parameters,

$$\hat{\boldsymbol{\Pi}} \equiv \frac{N_\delta}{p}\boldsymbol{\Pi}, \; \hat{\Delta} \equiv \frac{N_\delta}{p}\Delta, \; \hat{\mathbf{Q}} \equiv \frac{N_\delta}{p}\frac{\mathbf{Q}}{\sqrt{T/(2\varepsilon)}}, \; \nabla\hat{\mathbf{u}} \equiv -2\mu\frac{N_\delta}{p}\nabla\mathbf{u}, \tag{23}$$

$$N_\delta \equiv \frac{\mu_r u_r / L}{p_r} = \frac{\gamma M^2}{\mathrm{Re}} = \mathrm{Kn}\, M\sqrt{\frac{2\gamma}{\pi}}, \; \varepsilon \equiv \frac{1}{Ec\,\mathrm{Pr}}\frac{1}{T_r/\Delta T}.$$

The second-order nonlinear coupling factor $q_{2\mathrm{nd}}(c\hat{R})$ and the Rayleigh-Onsager dissipation function $\hat{R}$ are given by

$$q_{2\mathrm{nd}}(c\hat{R}) = \frac{\sinh(c\hat{R})}{c\hat{R}}, \quad \hat{R}^2 \equiv \hat{\boldsymbol{\Pi}}:\hat{\boldsymbol{\Pi}} + \frac{2\gamma'}{f_b}\hat{\Delta}^2 + \hat{\mathbf{Q}}\cdot\hat{\mathbf{Q}}. \tag{24}$$

Here $\gamma' = (5-3\gamma)/2$. The constant c, which is given by $c = \left[{}^{2\sqrt{\pi}}\!/_{5}\, A_2(\nu)\Gamma\left(4-{}^{2}\!/_{\nu-1}\right)\right]^{1/2}$, has a value between 1.0138 (Maxwellian) and 1.2232 ($\nu = 3$); for instance, 1.018 for the nitrogen gas molecule.[25] The tabulated values of $A_2(\nu)$ are available in the literature.[34] Note also that, once $q_{2\mathrm{nd}}(c\hat{R})$ is taken first-order, that is, $q_{1st} = 1$, and all coupled terms in the right hand side are neglected, the constitutive models (21) exactly recover the NF models (18) or (22).

Figure 2 illustrates the general features of the second-order constitutive relations (21) for diatomic and polyatomic gases in the one-dimensional compression-expansion and shear flows. The second-order constitutive model gives the asymmetrical behaviour of normal stress for the rapid expansion and compression of gas, as shown in Fig. 2(a). Even though the details of the second-order constitutive models for monatomic and diatomic and polyatomic gases are different, the general patterns remain unchanged. As the shear velocity gradient becomes very large the shear stresses predicted by the second-order constitutive model become very small, compared to the first-order

constitutive model, as shown in Fig. 2(b). Interestingly, Figs. 2(a) and (b) show the free-molecular asymptotic behaviour with increasing degree of expansion and velocity-shear, satisfying $\hat{\Pi}_{xx} + \hat{\Delta} \to -1$ or $\Pi_{xx} + \Delta + p \to 0$. Previous studies[25,26,35] showed that the solutions of the second-order constitutive models were well-posed (existence, uniqueness, and continuous dependence on the data) for all inputs on thermodynamic forces.

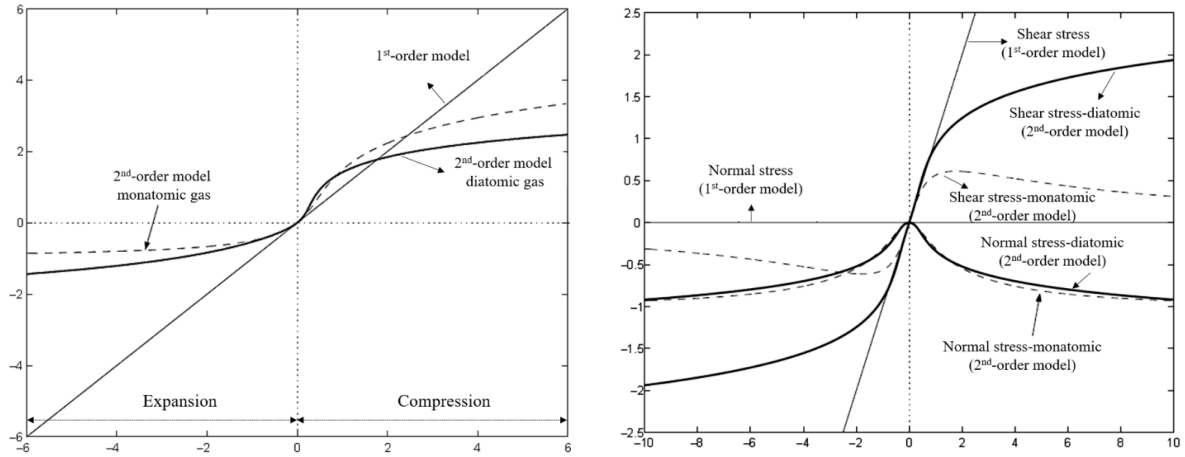

(a) Compression-expansion (b) Shear flow

FIG.2. Constitutive relations for monatomic and diatomic gases in (a) compression - expansion flow, and (b) shear flow. The horizontal axis represents the thermodynamic force by velocity gradient $\hat{\Pi}_0$, while the vertical axis represents the normal stress $\hat{\Pi}$. (Reproduced with permission from "A generalized hydrodynamic computational model for rarefied and microscale diatomic gas flows," Journal of Computational Physics, **195**, 655(2004). Copyright 2004 Elsevier Publication)

C. The numerical method based on an explicit modal discontinuous Galerkin method

The conservation laws (15) in conjunction with both first-order and second-order constitutive models, (18) and (21), are solved by an in-house mixed explicit structured discontinuous Galerkin (DG) method implemented in the serial platform, extended from the method originally developed for a monatomic gas by Xiao and Myong.[24, 36] The domain is decomposed using linear quadrilateral elements, and the scaled Legendre basis functions are employed for elements. The Gauss-Legendre quadrature rule was implemented for both the volume and the boundary integrations, and the local Lax–Friedrichs (LLF) flux was applied for inviscid terms, while the BR1 scheme[37] was employed for the auxiliary and viscous fluxes at elemental interfaces. A polynomial expansion of third-order accuracy was used to approximate solutions in the finite element space, and the third-order total

variation diminishing Runge-Kutta (TVD-RK) scheme was used for the time integration. To eliminate the spurious numerical fluctuations of the solutions, the nonlinear total variation bounded (TVB) limiter proposed by Cockburn and Shu was used.[38]

The right and left boundaries of the computational domain were set as an outflow condition, and as the moving shock Mach number and the associated thermodynamic condition specified by the Rankine-Hugoniot relations, respectively. The upper and lower boundaries were set based on flow conditions: before and after the shock wave. Since the shock wave is moving, the upper and lower boundaries are updated in every time step. The initial quiescent state surrounding the vortex had a pressure of 1013 Pa and a temperature of 273°K. In this study, three gases—argon, nitrogen and methane—are considered.

D. Important physical quantities in the SVI problem

1. Sound pressure

The sound pressure defined below is used to examine the basic structure of vortex deformation;

$$\Delta p = \frac{p - p_s}{p_s}, \tag{25}$$

where p is the local pressure and p_s is the pressure after the shock wave.

2. Rayleigh-Onsager dissipation function

The Rayleigh-Onsager dissipation function is used to measure the degree of non-equilibrium in flow fields;

$$\hat{R}^2 \equiv \hat{\boldsymbol{\Pi}} : \hat{\boldsymbol{\Pi}} + \frac{2\gamma'}{f_b}\hat{\Delta}^2 + \hat{\mathbf{Q}} \cdot \hat{\mathbf{Q}}. \tag{26}$$

3. Vorticity

The vorticity plays a vital role in understanding the interaction of a vortex with the shock wave. It can be defined as

$$\Omega_z = \frac{\partial v}{\partial x} - \frac{\partial u}{\partial y}. \tag{27}$$

4. Enstrophy evolution

The physical phenomena of vorticity generation or attenuation during the interaction can be explained by monitoring the time evolution of the enstrophy. The time evolution of the enstrophy can be defined as the area integral of the square of the vorticity in the flow field,[23]

$$\text{Enstrophy}(t) = \int_{\partial \text{A}} \Omega_z^2(x, y, t)\, dxdy, \tag{28}$$

where ∂A is the area of the computational domain.

5. Dissipation rate evolution

The viscous effects of diatomic and polyatomic gases can be investigated by introducing the area-weighted dissipation rate of kinetic energy

$$\text{Dissipation rate}(t) = \int_{\partial \text{A}} E(x, y, t)\, dxdy. \tag{29}$$

Here $E(x, y, t)$ denotes the dissipation rate per unit volume and is defined as

$$E(x, y, t) = -\left((\Pi_{xx} + \Delta) S_{xx} + \Pi_{xy} S_{xy} + \Pi_{yx} S_{yx} + (\Pi_{yy} + \Delta) S_{yy}\right), \tag{30}$$

where Π_{ij} is the viscous shear stress, Δ is the excess normal stress and S_{ij} is the strain rate defined as $S_{ij} = \partial u_i / \partial x_j$.

6. Vorticity transportation

The transport equation of vorticity can describe the dominant physics in the SVI since it contains several physically distinctive quantities.[23,31] The transport equation of vorticity can be written as the following in the two dimensional case,

$$\begin{aligned} \frac{\partial \Omega_z}{\partial t} = & -\Omega_z \left(\frac{\partial v}{\partial x} + \frac{\partial u}{\partial y} \right) + \frac{1}{\rho^2} \left(\frac{\partial \rho}{\partial x} \frac{\partial p}{\partial y} - \frac{\partial \rho}{\partial y} \frac{\partial p}{\partial x} \right) + \\ & \left[\frac{\partial}{\partial y} \left(\frac{1}{\rho} \frac{\partial}{\partial x} (\Pi_{xx} + \Delta) + \frac{1}{\rho} \frac{\partial \Pi_{xy}}{\partial y} \right) - \frac{\partial}{\partial x} \left(\frac{1}{\rho} \frac{\partial \Pi_{yx}}{\partial x} + \frac{1}{\rho} \frac{\partial}{\partial y} (\Pi_{yy} + \Delta) \right) \right]. \end{aligned} \tag{31}$$

There are three important dynamic processes for the vorticity component, Ω_z; (i) vorticity generation through the dilatation strain rate, (ii) baroclinic generation through the interaction of pressure and density gradients, and (iii) viscous vorticity generation through the viscous effects. The net area-weighted vorticity generation is defined as

$$\text{Net vorticity}(x,y,t) = \int_{\partial A} \frac{\partial \Omega_z}{\partial t} dxdy. \tag{32}$$

The net area-weighted dilatational vorticity generation is computed as follows:

$$\text{Dilatational vorticity}(x,y,t) = -\int_{\partial A} \Omega_z \left(\frac{\partial u}{\partial x} + \frac{\partial v}{\partial y} \right) dxdy. \tag{33}$$

The net area-weighted baroclinic vorticity generation is given as

$$\text{Baroclinic vorticity}(x,y,t) = \int_{\partial A} \frac{1}{\rho^2} \left(\frac{\partial \rho}{\partial x}\frac{\partial p}{\partial y} - \frac{\partial \rho}{\partial y}\frac{\partial p}{\partial x} \right) dxdy. \tag{34}$$

The net area-weighted viscous vorticity generation is expressed as

$$\begin{aligned} \text{Viscous vorticity}(x,y,t) = & \int_{\partial A} \frac{\partial}{\partial y} \left(\frac{1}{\rho}\frac{\partial}{\partial x}\left(\Pi_{xx} + \Delta\right) + \frac{1}{\rho}\frac{\partial \Pi_{xy}}{\partial y} \right) dxdy \\ & - \int_{\partial A} \frac{\partial}{\partial x} \left(\frac{1}{\rho}\frac{\partial \Pi_{yx}}{\partial x} + \frac{1}{\rho}\frac{\partial}{\partial y}\left(\Pi_{yy} + \Delta\right) \right) dxdy. \end{aligned} \tag{35}$$

III. GRID REFINEMENT STUDY AND VALIDATION OF THE NUMERICAL CODE

A. Grid refinement study

To evaluate the quality of the computational results, a grid refinement study was carried out by computing a macro SVI test case with $M_s = 1.5, M_v = 0.8, r_1 = 1000\lambda$ for nitrogen gas. A sequence of grids was considered: 100×100, 200×200, 400×400, and 800×800. The density contours of the macro SVI at 1000 nanoseconds were compared in Fig. 3. In addition, the density and pressure profiles at center-line of the domain for constant *y* and *x* were shown in Fig. 4 to demonstrate the grid sensitivity. The results show that there is no significant difference between the results obtained with the 400×400, and 800×800 grids, implying that the 800×800 grids were very close to asymptotic range. Based on this finding, all the computations were carried out on 800×800 grids.

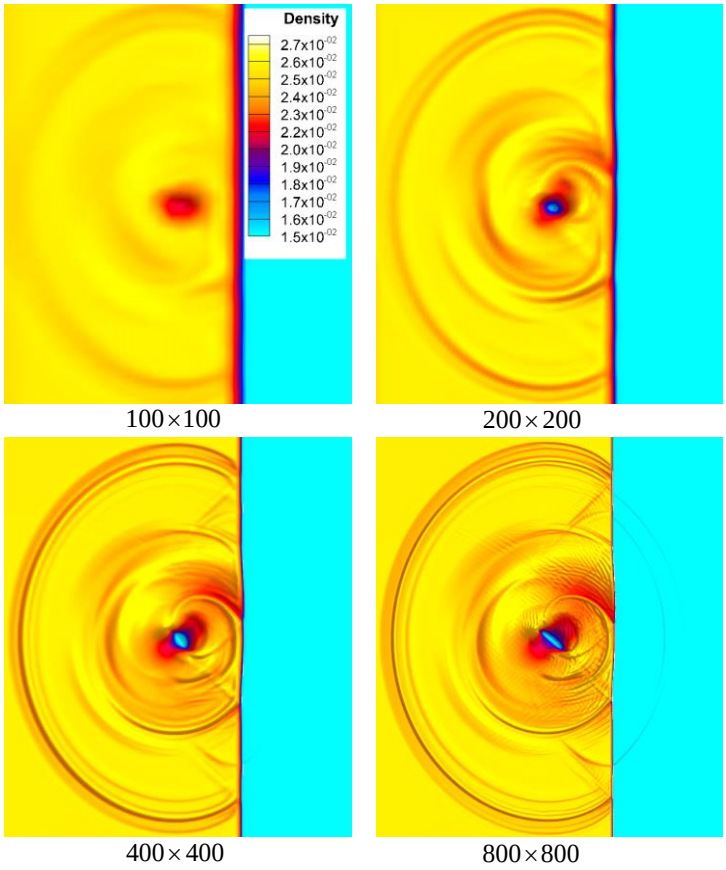

FIG. 3. Grid refinement study: density contours in macro SVI with $M_s = 1.5, M_v = 0.8$, $r_1 = 1000\lambda$, and $f_b = 0.8$ at $t = 1000$ ns.

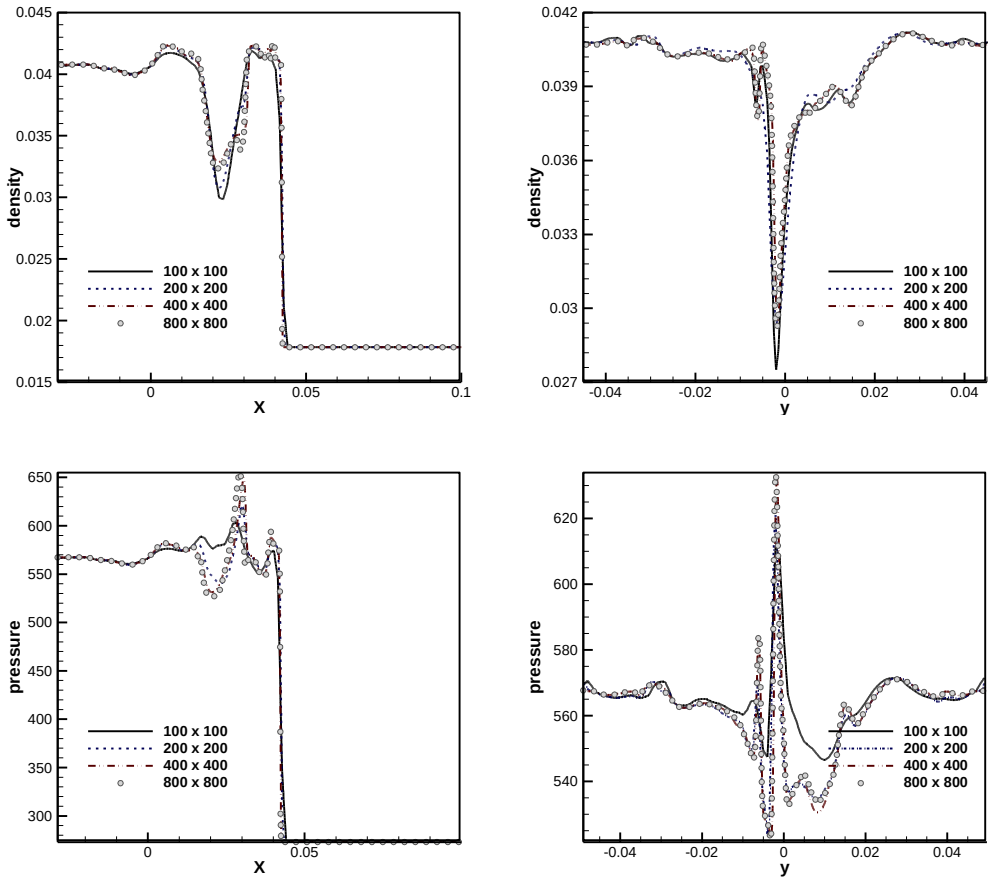

FIG. 4. Grid refinement study: density (upper) and pressure (below) profiles at center-line of domain in macro SVI with $M_s = 1.5, M_v = 0.8$, $r_1 = 1000\lambda$, and $f_b = 0.8$ at $t = 1000$ ns.

B. Validation of the numerical code

In order to verify the reliability and accuracy of the present computational model and numerical DG solver, we compared the computational results with the experimental data of Dosanjh and Weeks,[39] the theoretical results of Ribner,[14] and the computational results of Ellzey *et al.*[15] and Inoue and Hattori.[16] The conditions for this benchmark case were set based on the experimental study of Dosanjh and Weeks[39]; $M_s = 1.29, M_v = 0.39, \gamma = 1.4$.

Figure 5 shows a comparison of the circumferential distributions of the pressure amplitude defined as $\left(p_2 - p_p\right)/p_s$, where $p_p, p_2,$ and p_s denote the peak pressure of the precursor, the peak pressure of the second sound, and the pressure behind the shock wave, respectively. As seen from Fig. 5, the present result is very close to both the computational results of Ellzey *et al.*[15] and Inoue and Hattori.[16]

This indicates that the present numerical code is able to compute the flow-fields in macro SVI accurately.

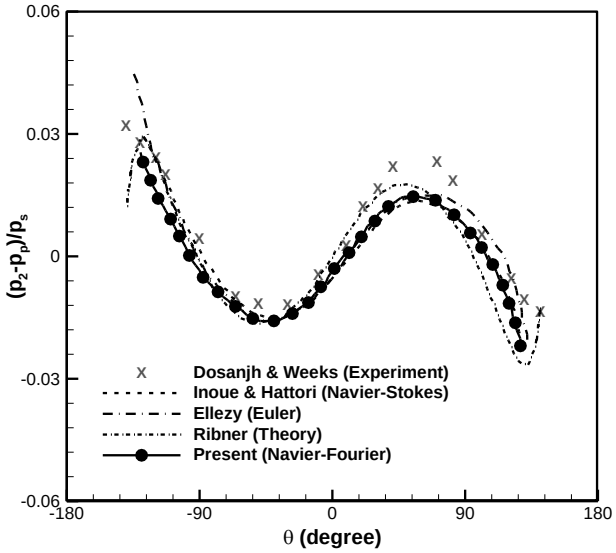

FIG. 5. First-order (Navier-Fourier) constitutive model validation: circumferential distribution of the pressure amplitude in macro SVI (air).

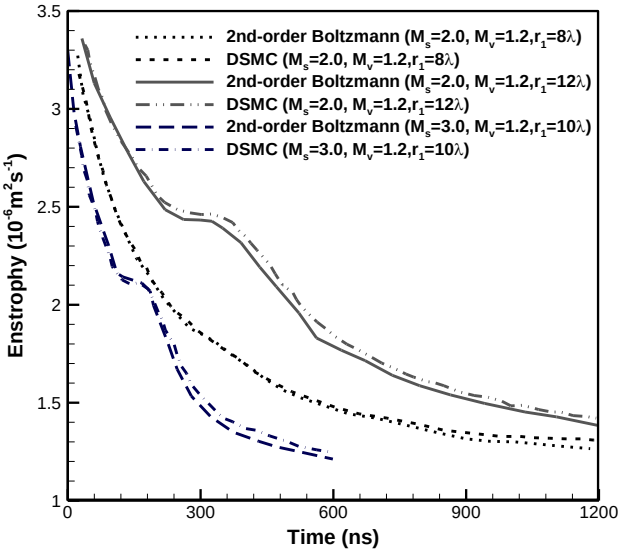

FIG. 6. Second-order Boltzmann based constitutive model validation: time evolution of area-weighted enstrophy in micro SVI (argon gas).

In order to further check the present second-order Boltzmann-Curtiss-based constitutive model, three different cases of micro SVI investigated by Koffi *et al.*[23] were considered. Argon gas in its quiescent state surrounding the vortex at an initial temperature of 273 K and an initial pressure of

1013 Pa was considered. The core radius varied from 8λ to 12λ. In Fig. 6, the time of the enstrophy is compared with the DSMC results. It can be seen from Fig. 6, that the present results, including the general trend of the enstrophy change with time, are found very close to the DSMC study of Koffi *et al.*,[23] which used argon molecules, variable hard sphere (VHS) inter-particle model, 25 particles in each cell, and time step size of 2×10^{-9}.

IV. RESULTS OF EFFECTS OF DIATOMIC AND POLYATOMIC GASES ON THE SVI, AND DISCUSSION

In this section, we investigate the physics of the macro and micro SVIs in diatomic and polyatomic gases, in particular, in relation to the non-equilibrium effects. Emphasis is placed on the sound generation mechanism, vorticity transport, enstrophy evolution, and dissipation rate evolution. Three types of vortices were chosen for extensive studies, including a transonic vortex with $M_v = 1.0$ followed by two types of subsonic vortices with $M_v = 0.6$ and $M_v = 0.8$. For the given vortex Mach number, the core radius increases from 8λ to 1000λ with a step of 2λ. The incident shock Mach number M_s increases from 1.5 to 3.5 with a step of 0.5. Three gases were considered to investigate the non-equilibrium effects of diatomic and polyatomic gases; argon ($f_b = 0.0$), nitrogen ($f_b = 0.8$), and methane ($f_b = 1.33$). A road map of the simulation cases for the SVI is presented in Fig. 7.

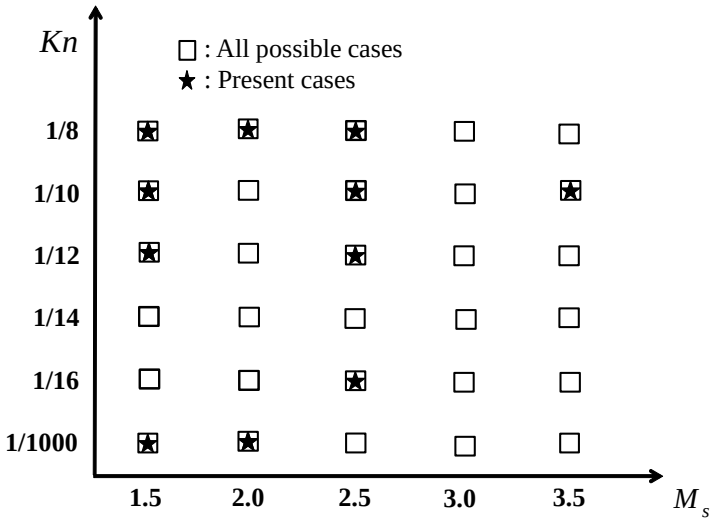

FIG. 7. Road map of simulation cases of present SVI study with $M_v = 0.6, 0.8, 1.0$; and $f_b = 0.0,\ 0.8,\ 1.33$.

A. Sound generation mechanism in the SVI for diatomic and polyatomic gases

The sound generation mechanism is considered the most interesting phenomena in the SVI. To understand this phenomenon, we conducted an extensive investigation on the time evolution of sound pressure in the macro and micro SVIs of diatomic and polyatomic gases.

1. Sound generation mechanism in the macro SVI

Figure 8 displays the time evolution of sound pressure in the macro SVI with conditions $M_s = 2.0, M_v = 0.8,\ r_1 = 1000\lambda,$ and $f_b = 1.33.$ The symbol '+' denotes the compression region while '-' presents the rarefaction region. As the incident shock wave interacts with the outer flow field of the clockwise-rotating composite vortex, the lower and upper portions of the incident shock wave are diffracted around the vortex. The two diffracted shocks, a fast diffracted shock (FD) and a slow diffracted shock (SD), are connected by the refracted shock (RF), which passes through the vortex core, as shown in Fig. 8(a). A rarefaction region appears in the upper portion where the shock propagation is promoted by the vortex velocity, while a compression region appears in the lower portion where the shock propagation is deterred by the vortex velocity. As a result, a precursor is generated first, as seen in Fig. 8(a). As the interaction develops, the incident shock wave passes though the vortex core and is distorted into an S shape, as shown in Fig. 8(b). New rarefaction and compression regions appear outside of the compression and rarefaction regions, respectively. This process of interaction shows that the precursor changes from an initially dipolar to a quadrupolar nature consisting of compressions and rarefactions along the circumferential direction.

Figure 8(c) shows that, when the incident shock wave passes through the vortex flow field, a Mach reflection configuration is generated with two reflection shocks MR1 and MR2, which propagate upward and downward, respectively. Because of the clockwise rotation of the vortex, both the strength and propagating velocity of MR2 is larger than that of MR1. At the same time, a second acoustic wave appears behind the precursor, which also displays a quadrupolar nature. The Mach stem MS accelerates relative to the two incident shocks waves SW1 and SW2, and the shock front again becomes approximately planar as shown in Fig. 8(d). A shocklet type shock wave C1 is also observed

at the opposite side of vortex core which merges with the planar shock front part as seen in Figs. 8(e) and 8(f). Further, another two reflection shocks MR3 and MR4 are formed, moving upward and downward, respectively. Finally, a third sound wave with a quadrupolar nature is generated by the compressed vortex, as shown in Fig. 8(f).

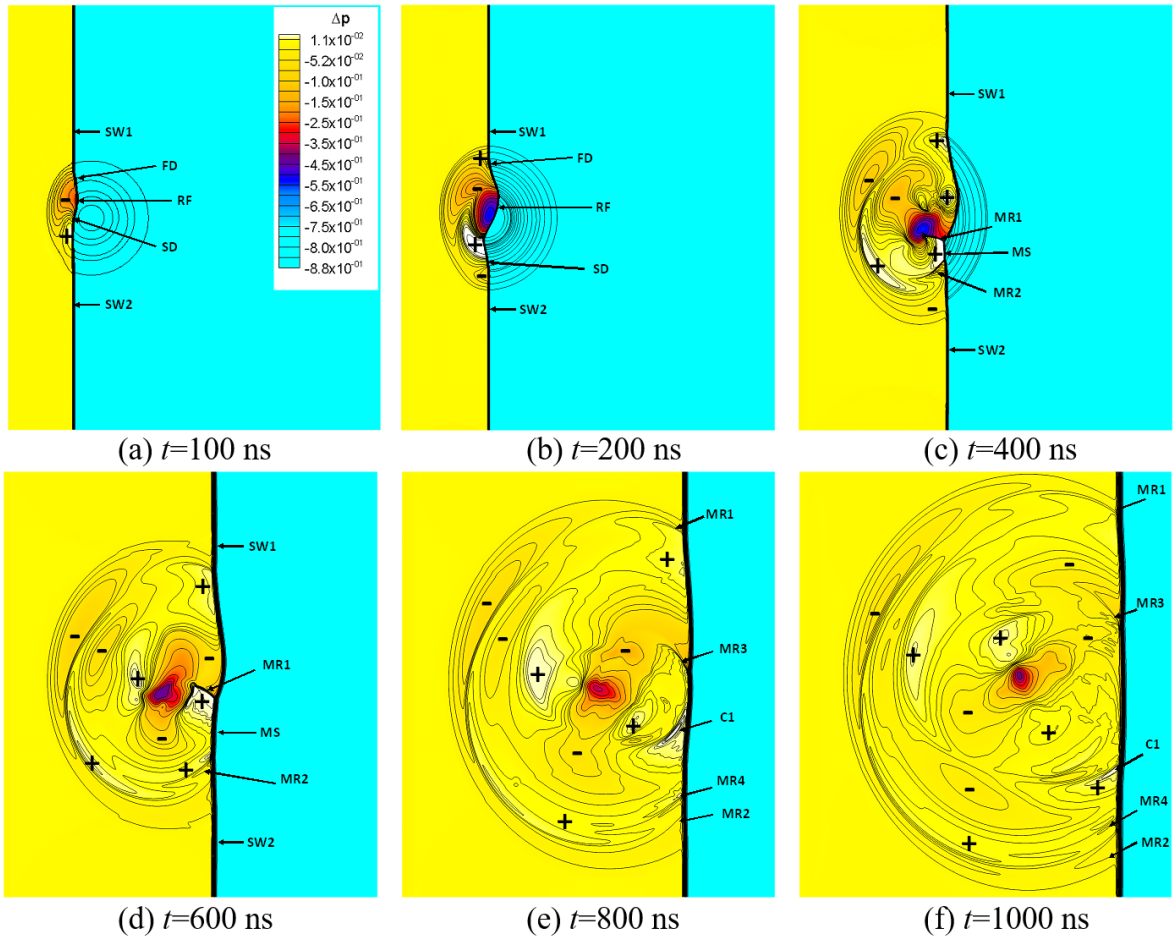

FIG. 8. Time evolution of sound pressure for macro SVI with $M_s = 2.0, M_v = 0.8$, $r_1 = 1000\lambda$, and $f_b = 1.33$.

2. *Sound generation mechanism in micro SVI*

Figure 9 displays the time evolution of sound pressure in the micro SVI with conditions $M_s = 2.0, M_v = 0.8$, $r_1 = 10\lambda$, and $f_b = 1.33$. As the incident shock wave interacts with the outer flow field of the micro vortex, the lower and upper portion of the shock wave are diffracted slowly around the vortex, as seen in Fig. 9(a). One rarefaction region is developed in the upper and lower portions of

the incident shock wave. When the incident shock wave approaches the vortex core, a compression region is generated between the two rarefaction regions.

Also, a Mach stem MS and two reflected shock waves MR1 and MR2 are formed, as shown in Fig. 9(b). Later, as the incident shock wave passes through the vortex core, new rarefaction and compression regions appear outside the rarefaction regions in the upper portion of the shock wave, as shown in Fig. 9(c). Because the vortex rotates in a clockwise direction, the deformed incident shock wave SW1 moves upward and one compression region is developed near the upper side of the vortex core, as shown in Fig. 9(d). For the same reason, the strength of reflected shock wave MR2 is stronger than that of MR1. Further, two additional shock waves MR3 and MR4 are formed and one rarefaction region comes out near the vortex core, as demonstrated in Fig. 9(e). This rarefaction region moves upward near the compression region and a second sound wave is generated, as seen in Fig. 9(f).

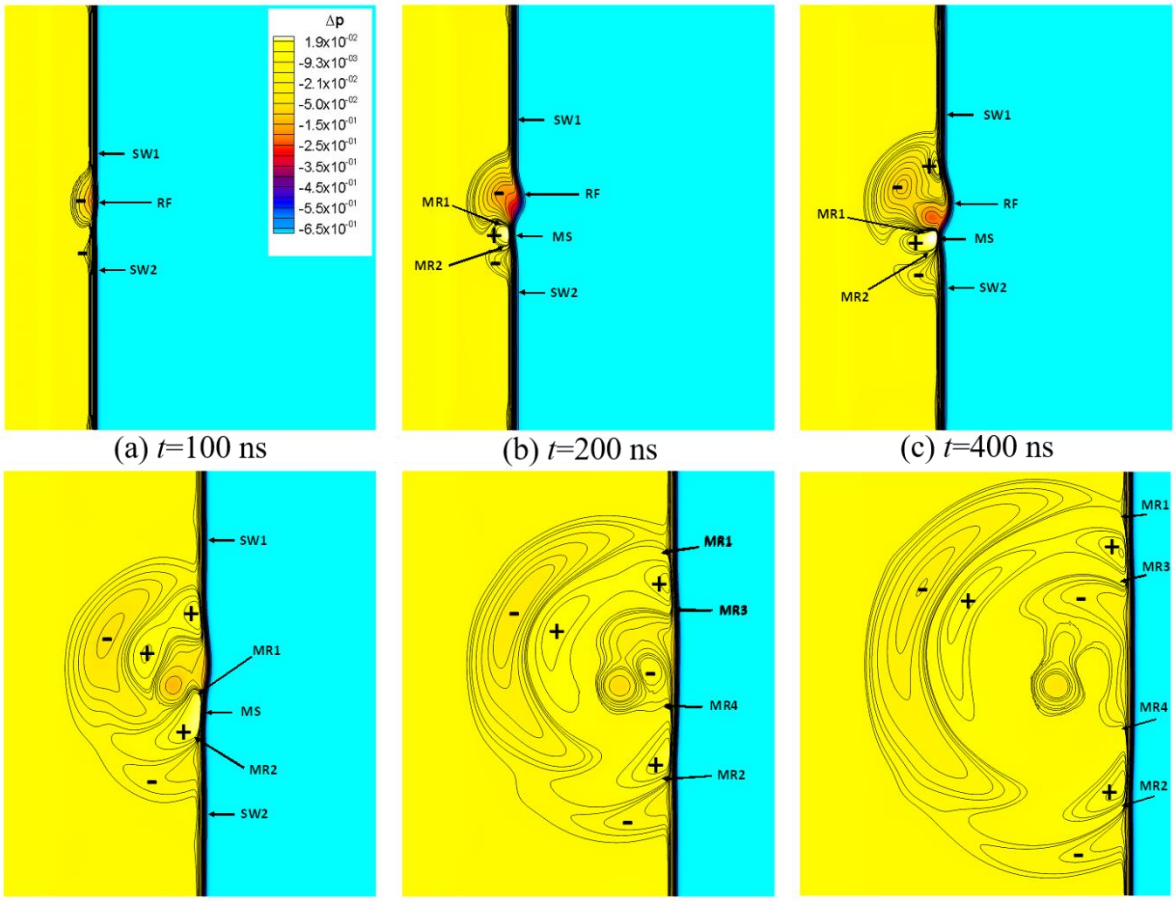

(a) t=100 ns (b) t=200 ns (c) t=400 ns

(d) t=600 ns (e) t=800 ns (f) t=1000 ns

FIG. 9. Time evolution of sound pressure for macro SVI with $M_s = 2.0, M_v = 0.8$, $r_1 = 10\lambda$, and $f_b = 1.33$.

Overall, the results show that the micro SVI has an evolving pattern of sound pressure similar to the macro SVI. However, due to the enhanced viscous dissipations in the micro SVI, the pattern is much more smeared, including the incident, reflected and newly formed shock waves. For a similar reason, *it was observed that the quadrupolar acoustic wave structures, which are typical in the macro SVI, disappear in the micro SVI.*

From Ribner's linearized theory of SVI[14] which predicts the quadrupolar acoustic wave in a macro SVI, the pressure jump varies around the vortex and generates a quadrupole field. The interaction also causes a $1/r$ potential flow around the vortex core and the pressure of this potential flow field can be expressed as

$$p \sim \frac{u_{\mathrm{m}}}{\mathrm{V}}\left(\frac{r_1}{at}\right)^{1/2}. \tag{36}$$

Here V is the upstream velocity of the shock. The expression (36) conforms that when the radius of the vortex core r_1 is very small, the pressure jump is greatly weakened in the micro SVI. As a result, the quadrupolar acoustic wave disappears in the micro SVI.

B. Effects of diatomic and polyatomic gases on the macro and micro SVIs

Here we investigate the effects of diatomic and polyatomic gases on the macro and micro SVIs. For this purpose, we selected three gases: monatomic argon $(f_b = 0.0)$, diatomic nitrogen $(f_b = 0.8)$, and linear polyatomic methane $(f_b = 1.33)$. We basically considered two types of the SVI problem: macro SVI with $r_1 = 1000\lambda$, $M_v = 0.8$, and micro SVI with $r_1 = 10\lambda$, $M_v = 0.8$ for $M_s = 1.5,\ 2.0$.

1. Sound pressure

Figure 10 displays the effects of diatomic and polyatomic gases on the sound pressure in macro and micro SVIs at time t = 1000 ns. Due to the strong shock vortex interaction, a Mach reflection configuration is developed in all cases. In the monatomic case ($f_b = 0.0$) it is observed that a second sound wave and two reflected shock waves, MR1 and MR2, are generated in the macro SVI, as seen in Fig. 10(a). In addition, a small shocklet type wave C1 appears at the opposite side of the vortex

core and near a compression region. When the f_b value increases to 0.8, two additional reflected shock waves, MR3 and MR4, are formed and the shocklet wave C1 becomes larger in comparison with the monatomic case, as shown in Fig. 10(b).

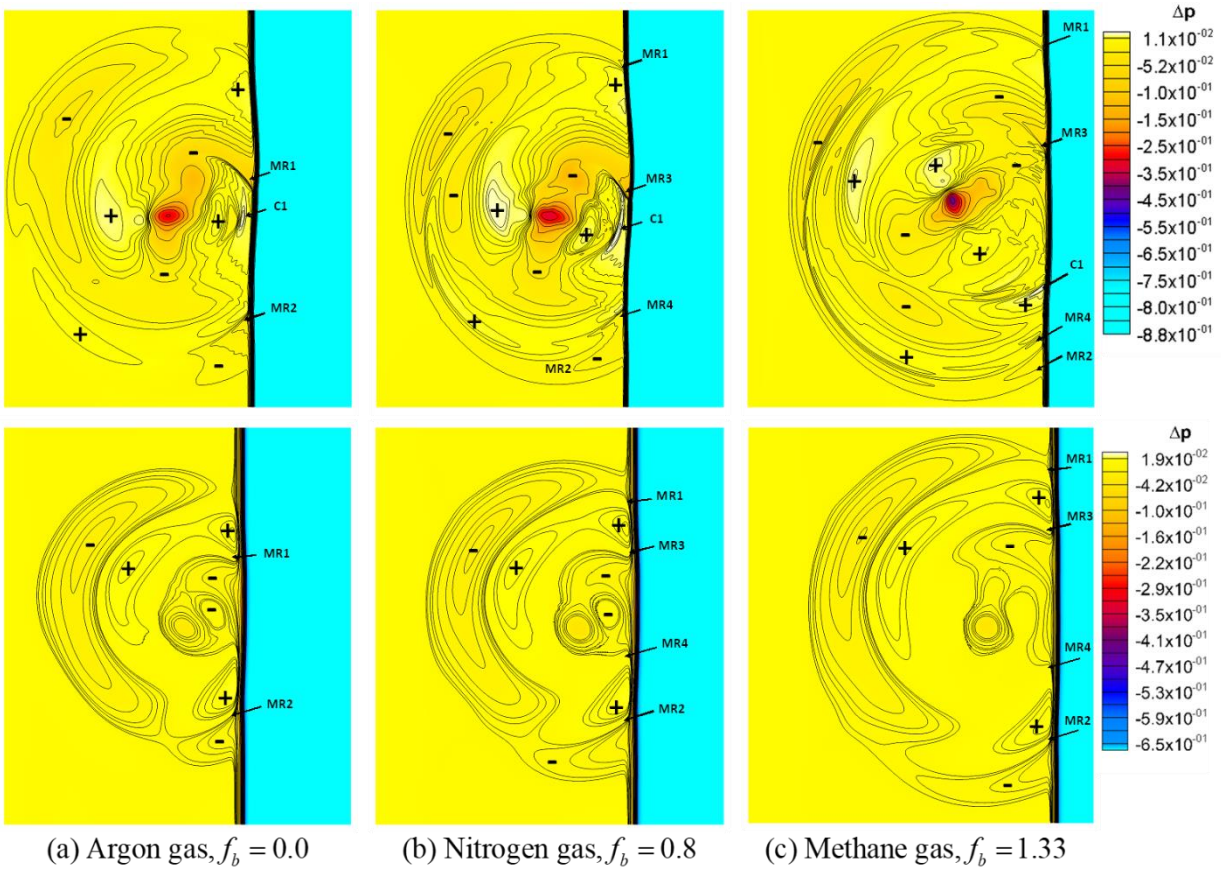

FIG. 10. Effects of diatomic and polyatomic gases on macro SVI with $M_s = 2.0, M_v = 0.8,\ r_1 = 1000\lambda$ (top) and micro SVI with $M_s = 2.0, M_v = 0.8,\ r_1 = 10\lambda$ (bottom): sound pressure at $t = 1000\,\text{ns}$.

Moreover, the strength of reflected shock waves is stronger than that of the reflected shock waves in the monatomic case. This difference is possibly due to the substantial contribution of the dilatational term appearing in the constitutive relations for the diatomic and polyatomic gases. As the f_b value increases further to 1.33, an additional (third) sound wave is generated, as shown in Fig. 10(c). The expansion region of the sound waves becomes larger with increasing f_b. It is also observed that the size of the shocklet wave C1 increases and begins to merge with the reflected shock waves of a quadrupolar nature.

On the other hand, the sound pressure pattern in the micro SVI is notably different from the macro SVI. First, the quadrupolar acoustic wave structure, which is the main feature of the macro SVI, is no

longer observed in the micro SVI. Second, no shocklet type waves exist in the micro SVI. Nevertheless, faster propagation of the incident shock wave with increasing f_b (equivalently, decreasing γ) was observed in both the macro and micro SVIs, since the shock propagation speed is affected by the specific heat ratio of the gases, regardless of the macro or micro condition.

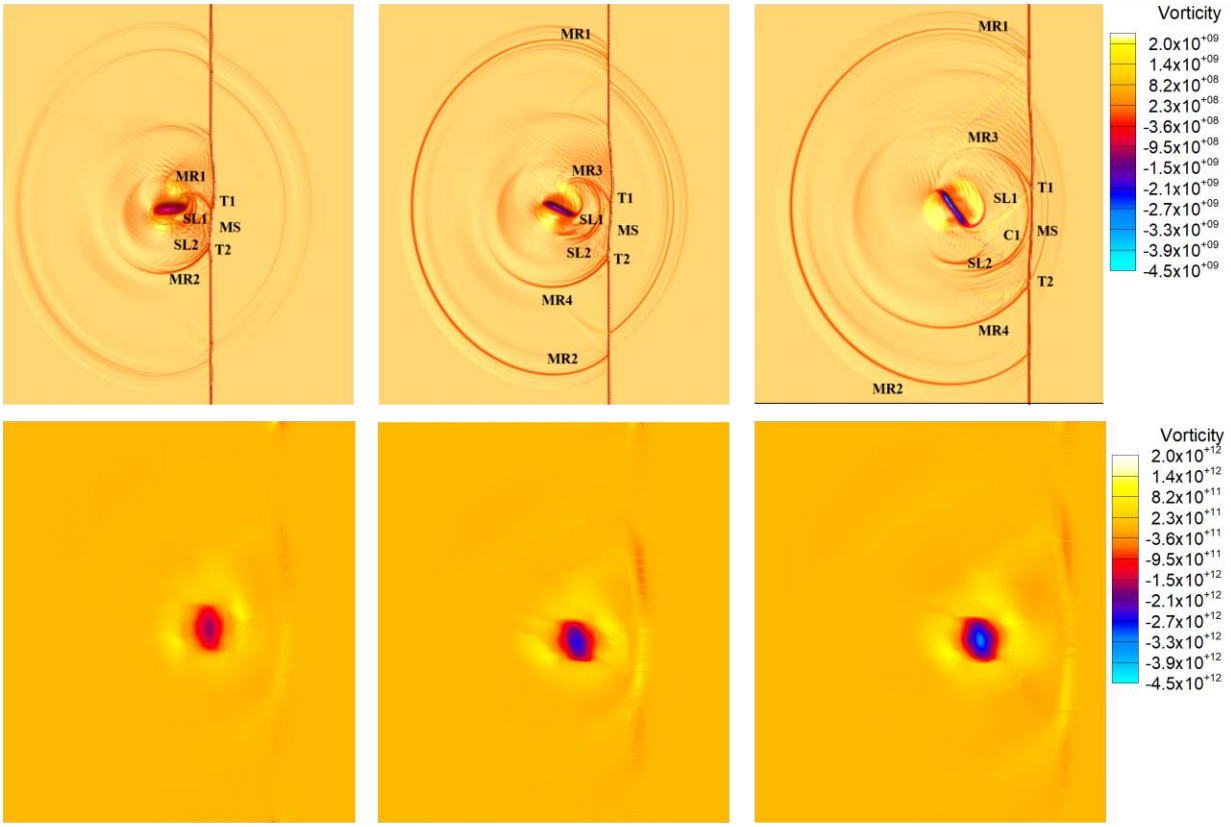

(a) Argon gas, $f_b = 0.0$ **(b) Nitrogen gas, $f_b = 0.8$** **(c) Methane gas, $f_b = 1.33$**

FIG. 11. Effects of diatomic and polyatomic gases on macro SVI with $M_s = 1.5, M_v = 0.8$, $r_1 = 1000\lambda$ (top) and micro SVI with $M_s = 1.5, M_v = 0.8, r_1 = 10\lambda$ (bottom): vorticity contours at $t = 1000\,\text{ns}$.

2. Vorticity distribution

Figures 11-12 illustrate the effects of the diatomic and polyatomic gases on the vorticity distribution in the macro and micro SVIs for $M_s = 1.5, 2.0$ at time t=1000 ns. It can be easily observed that there are significant differences in vorticity distribution for the different gases after the interaction. For instance, as already explained in the subsection on sound pressure, two additional reflected shock waves, MR3 and MR4, are clearly formed in the macro SVI in the case of diatomic

and polyatomic gases. Furthermore, in the macro SVI, two branches of slip lines (SL1 and SL2) emanating from the vortex core are formed and it becomes strong with increasing Mach number and becomes weak with increasing f_b value.

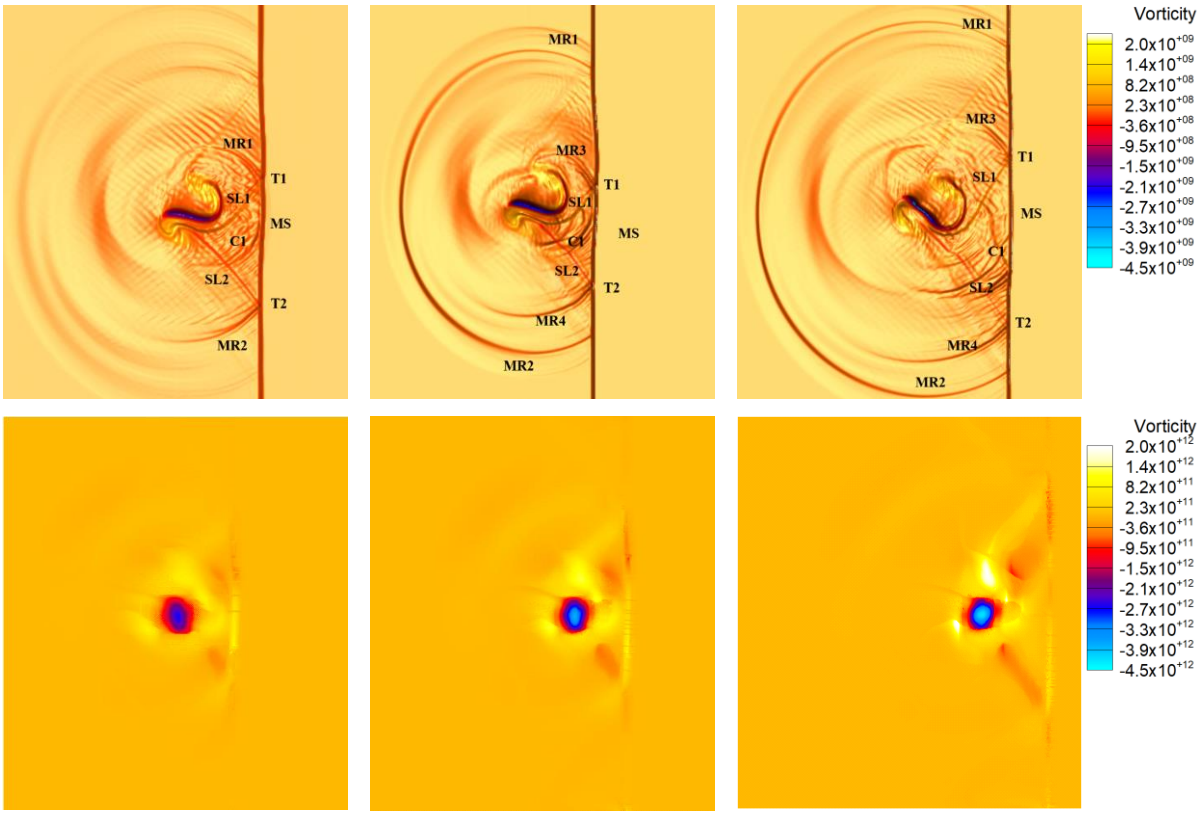

(a) Argon gas, $f_b = 0.0$ (b) Nitrogen gas, $f_b = 0.8$ (c) Methane gas, $f_b = 1.33$

FIG. 12. Effects of diatomic and polyatomic gases on macro SVI with $M_s = 2.0, M_v = 0.8$, $r_1 = 1000\lambda$ (top) and micro SVI with $M_s = 2.0, M_v = 0.8$, $r_1 = 10\lambda$ (bottom): vorticity contours at $t = 1000\,\text{ns}$.

In the present simulations, a composite vortex has negative vorticity in its core and positive vorticity on the outside, so that the total circulation produced by the regions may be zero. After the interaction, the vortex is deformed in a horizontally stretched form in the macro SVI, while it remains in a circular shape and is squeezed in the longitudinal direction in the micro SVI.

In the macro SVI with small f_b value, it is observed that the inner core of the vortex with negative vorticity is stretched and the outer annular region with positive vorticity begins to detach from the inner core, as shown in Figs. 11(a) and 12(a). This stretching is more pronounced for large f_b values, as seen from Figs. 11(b)(c) and 12(b)(c). It was also found that, with increasing f_b value, the domain

of negative vorticity increased, due to enhanced vorticity generation. For a shock Mach number of 1.5, as depicted in Fig. 11, due to weak shock strength, weak reflected shock waves are observed and the vortex core is less deformed in both the macro and micro SVIs. On the other hand, for shock Mach number 2.0, the vortex core is completely disrupted, in particular, in diatomic and polyatomic gases, as shown in Figs. 12(b)(c).

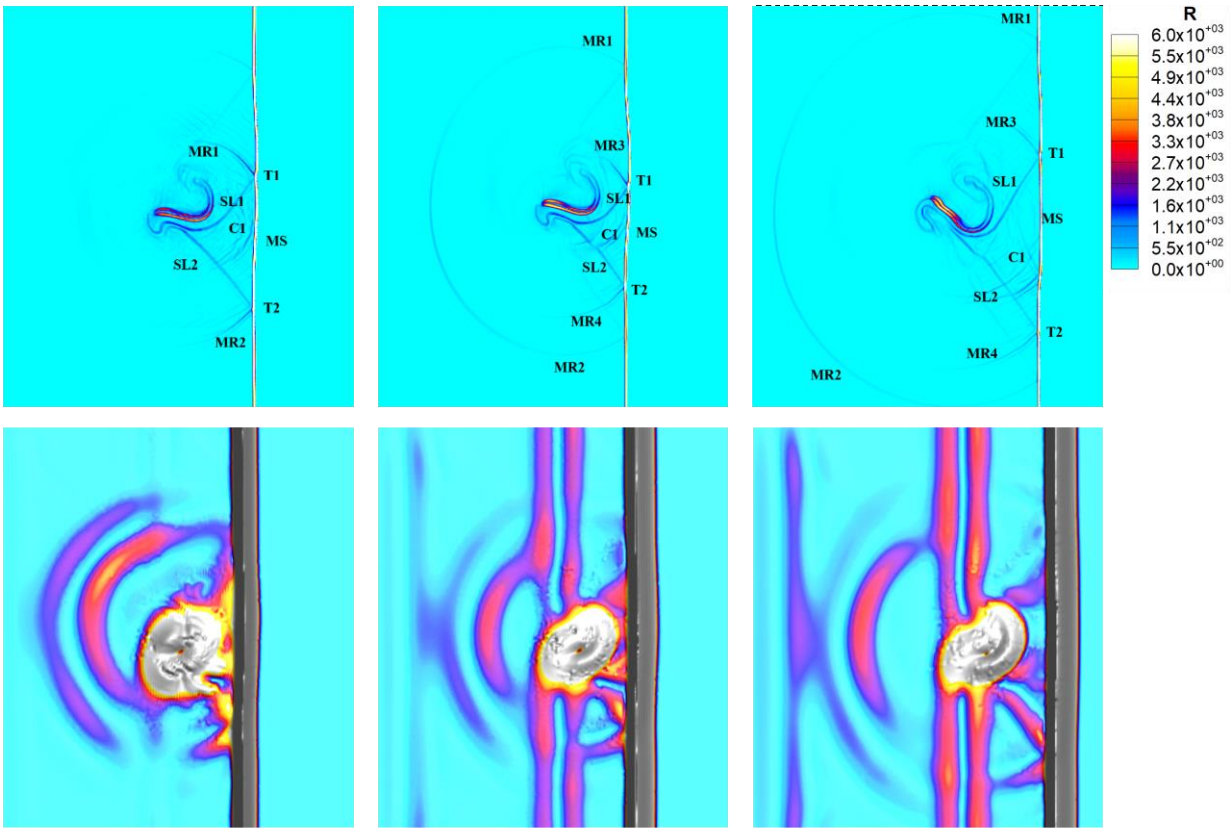

(a) Argon gas, $f_b = 0.0$ (b) Nitrogen gas, $f_b = 0.8$ (c) Methane gas, $f_b = 1.33$

FIG. 13. Effects of diatomic and polyatomic gases on macro SVI with $M_s = 2.0, M_v = 0.8$, $r_1 = 1000\lambda$ (top) and micro SVI with $M_s = 2.0, M_v = 0.8$, $r_1 = 10\lambda$ (bottom): degree of non-equilibrium contours at $t = 1000\,\text{ns}$.

3. Degree of thermal non-equilibrium

Figure 13 shows the effects of diatomic and polyatomic gases on the degree of thermal non-equilibrium in macro and micro SVIs at time t=1000 ns. The thermal non-equilibrium parameter R defined in (26) was calculated in order to examine what regions could be expected to deviate significantly from the local equilibrium state during the interaction. As expected, it was observed that

the degree of thermal non-equilibrium is very high in the micro SVI case compared with the macro SVI.

In general, the macro SVI shows a low degree of deviation from thermal equilibrium, and the deviation is mostly confined inside the shock and vortex regions. In contrast, the micro SVI is significantly affected by the non-equilibrium process in all types of gases, and the deviation occurs inside a much broader domain. It is apparent that the non-equilibrium process associated with the micro SVI affects a large portion of the flow field.

This result confirms the essence of the difference between the macro and micro SVI. Moreover, by comparing Figs. 12 and 13, it can easily be noticed that, while both the vorticity and the non-equilibrium parameter based on the Rayleigh-Onsager dissipation function can describe the essential features in the macro SVI quite effectively, the non-equilibrium parameter is much more effective than the vorticity in the case of the micro SVI.

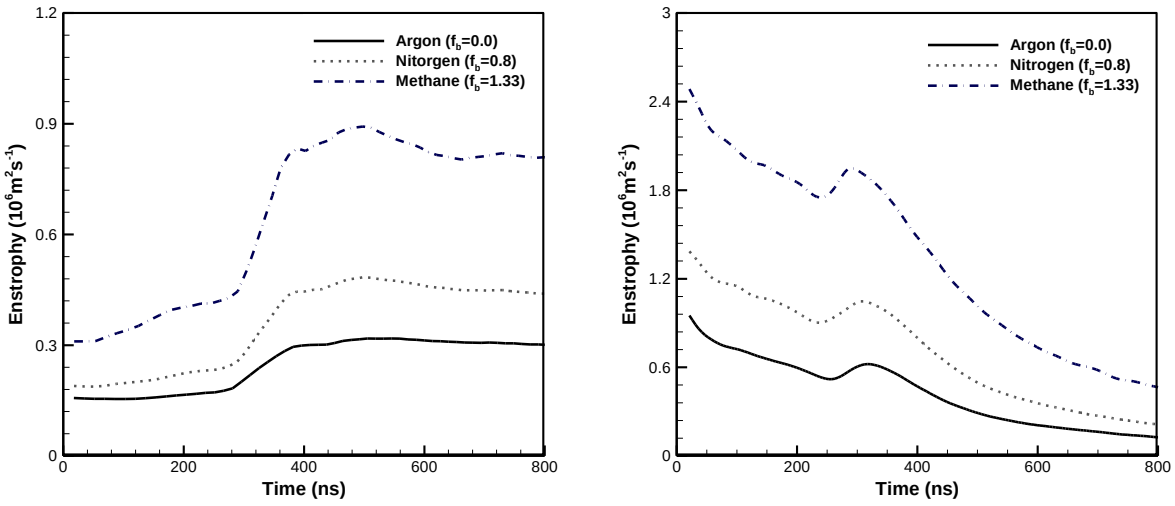

(a) (b)

FIG. 14. Effects of diatomic and polyatomic gases on (a) macro SVI with $M_s = 2.0, M_v = 0.8, r_1 = 1000\lambda$, and (b) micro SVI with $M_s = 2.0, M_v = 0.8, r_1 = 10\lambda$: time evolution of enstrophy.

4. Evolution dynamics

Figure 14 illustrates the effects of diatomic and polyatomic gases on the time evolution of enstrophy in the macro and micro SVIs. It can be seen that the enstrophy during the interaction is

substantially enhanced with increasing f_b value in both the macro and micro SVIs. However, a different pattern of enstrophy evolution is observed in the macro and micro SVIs.

In the macro SVI, the enstrophy increases until 400 ns and then remains fairly constant, as shown in Fig. 14(a). On the other hand, in the micro SVI, the enstrophy decreases rapidly until 250 ns and, after that, it increases briefly at 250-350 ns. Then it decreases slowly for the remainder of the interaction, as shown in Fig. 14(b).

The effects of diatomic and polyatomic gases can be further examined through the time evolution of the dissipation rate, shown in Fig. 15. It can be seen that the effect of the rotational mode in gases on the dissipation rate is reversed, depending on the macro or micro condition. Figure 15(a) indicates there is an increase in the dissipation rate with increasing f_b value in the macro SVI, whereas Fig. 15(b) shows the opposite trend for the micro SVI, a decrease in dissipation rate with increasing f_b value.

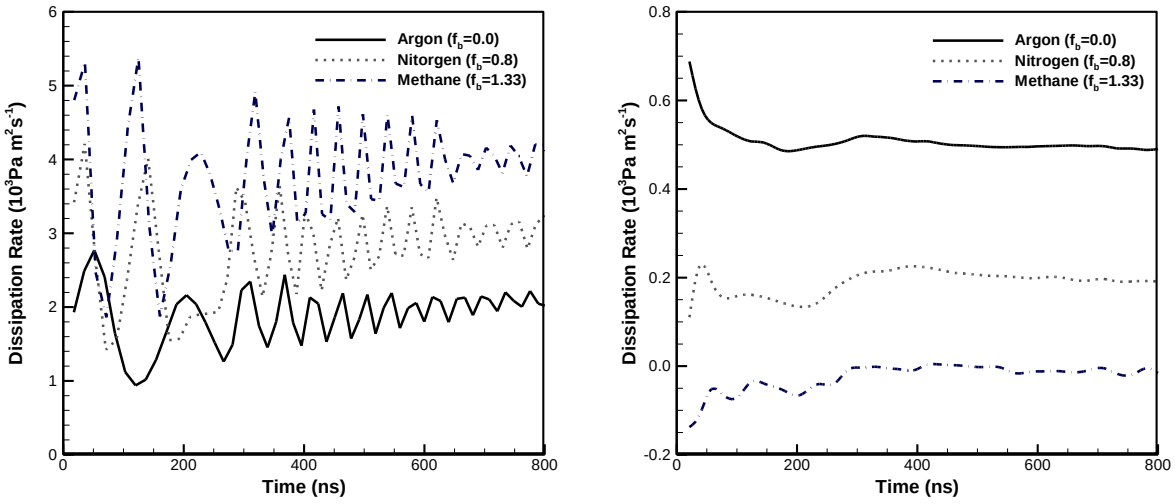

(a) (b)

FIG. 15. Effects of diatomic and polyatomic gases on (a) macro SVI with $M_s = 2.0, M_v = 0.8, r_1 = 1000\lambda$, and (b) micro SVI with $M_s = 2.0, M_v = 0.8, r_1 = 10\lambda$: time evolution of dissipation rate.

5. Summary of macro and micro SVIs in diatomic and polyatomic gases

Several major effects of diatomic and polyatomic gases on the shock-vortex interaction were identified; for example, the generation of additional reflected shock waves MR3 and MR4 were

observed in both the macro and micro SVIs for non-monatomic gases. A significant increase in enstrophy was also observed with increasing f_b value in both the macro and micro SVIs. Furthermore, the macro and micro SVIs showed distinct flow field features.

It is interesting to note that the quadrupolar acoustic wave structure, which is an essential phenomenon in the macro SVI, was not observed in any case of micro SVI.

Finally, the degree of thermal non-equilibrium was found to be very high in the micro SVI in comparison with the macro SVI, and consequently the non-equilibrium parameter is much more effective in describing the essential features in the micro SVI.

TABLE I. Simulation cases for flow pattern and vortex deformation (nitrogen).

Cases	Shock Mach (M_s)	Vortex Mach (M_v)	Core radius (r_1)
1	1.5	1.0	8λ
2	1.5	1.0	12λ
3	2.5	1.0	8λ
4	2.5	1.0	12λ

C. Characteristics of micro SVIs in diatomic and polyatomic gases

1. Vortex deformation through a shock wave

Vortex deformation by incident shock wave is a basic flow feature of the micro SVI. To analyse this physical phenomenon, four cases were selected, as summarized in Table I. These cases were chosen to demonstrate the effects of shock wave strength and vortex size on the interaction, and they may be considered as representative of the micro SVI. The first two cases involve a relatively weak shock wave, a vortex $(M_s = 1.5, M_v = 1.0)$, and different vortex sizes $r_1 = 8\lambda, 12\lambda$. In contrast, the last two cases involve a strong shock wave, a vortex $(M_s = 2.5, M_v = 1.0)$, and different vortex sizes $r_1 = 8\lambda, 12\lambda$. Nitrogen gas, a major component of air, was considered as a representative diatomic gas for the study of the micro SVI.

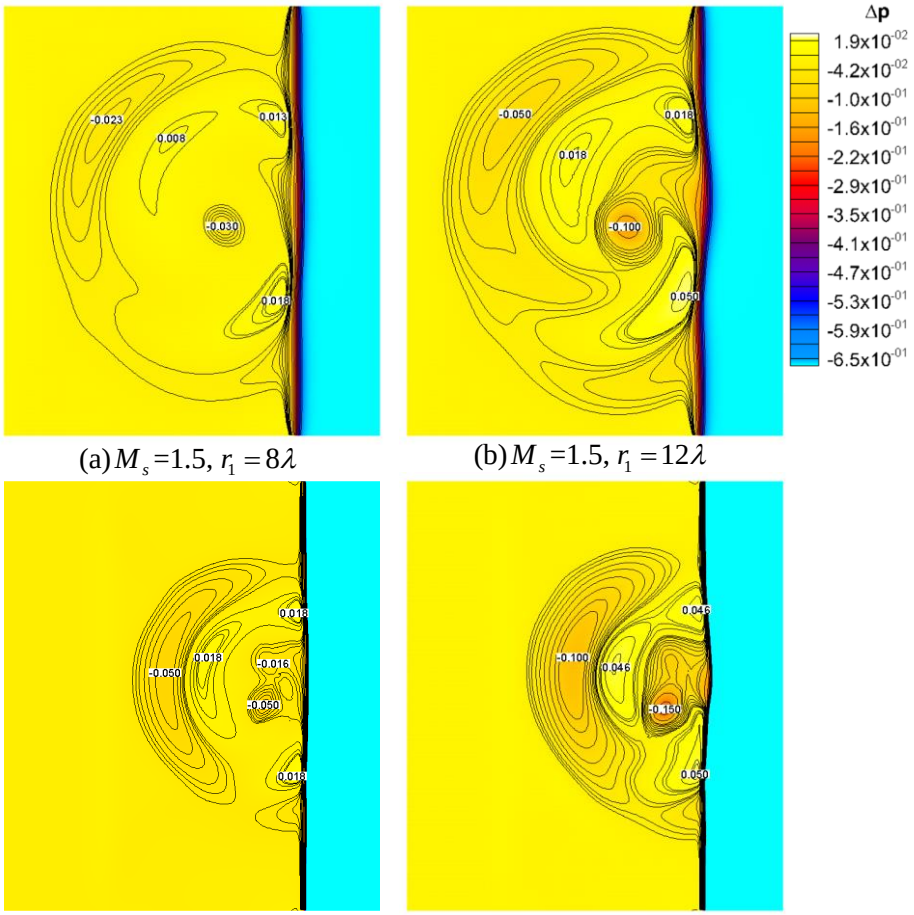

(a) M_s=1.5, $r_1 = 8\lambda$ (b) M_s=1.5, $r_1 = 12\lambda$

(c) M_s=2.5, $r_1 = 8\lambda$ (d) M_s=2.5, $r_1 = 12\lambda$

FIG. 16. Vortex deformation in micro SVI: sound pressure contours with M_v=1.0.

Figure 16 shows four snapshots of the sound pressure contours generated in the micro SVI with different incoming shock Mach numbers and vortex sizes. The positive value of the sound pressure denotes the compression region, whereas the negative value denotes the rarefaction region. The results show that five regions, two rarefication and three compression regions, are generated after the interaction in all cases. These regions are strongly dependent on the strength of the incoming shock wave. For example, the first two cases 1 and 2 produce three weak compression regions, while the last two cases 3 and 4 produce three strong compression regions, which are located between the two rarefaction regions. It can also be observed that stronger compression and rarefaction regions are produced at larger vortex sizes. It is interesting to note that the quadrupolar acoustic wave structure, which is the prime feature in the macro SVIs, is not found in any case of micro SVI.

The results show that vortex deformation produced by an incident shock wave is strongly dependent on the strength of the interaction. In this context, the information about the vorticity evolution during the interaction may be very helpful. It can be obtained by examining the evolution dynamics of the net production and dissipation of vorticity.

2. Evolution dynamics of micro SVIs

Figure 17 displays the time evolution of enstrophy and dissipation rate for all cases 1 - 4. A substantial attenuation of enstrophy with time is found in all cases, as shown in Fig. 17(a). The results show that the first two cases 1 and 2 with a weak shock wave produce an enstrophy pattern that is different from the last two cases 3 and 4 which have a strong shock wave. It may be noted that the shock wave in cases 1 and 2 starts to interact actively with the vortex around 200 ns and completes around 600 ns. Moreover, a monotonic decrease in enstrophy is found throughout the interaction process.

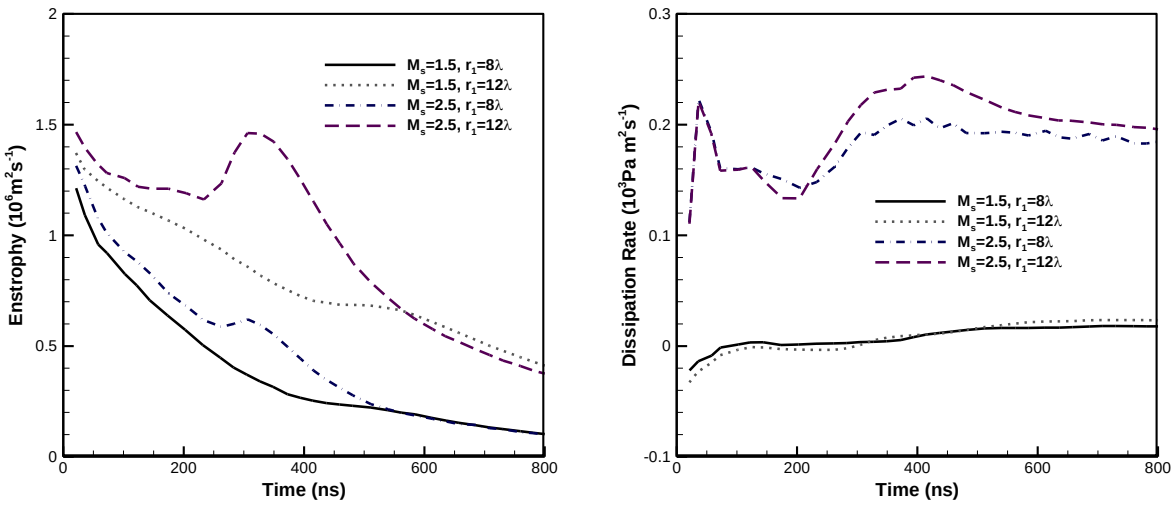

(a) (b)

FIG. 17. Vortex deformation in micro SVI: time evolution of (a) enstrophy and, (b) dissipation rate with M_v=1.0.

On the other hand, in cases 3 and 4, a brief increase in enstrophy is observed during the interaction process (250-400 ns). This difference can also be confirmed in the time evolution of the dissipation rate as shown in Fig. 17(b). The dissipation rate in cases 1 and 2 remains relatively constant over time

during the entire weak interaction process, whereas the dissipation rate in cases 3 and 4 experiences a substantial increase during the strong interaction process.

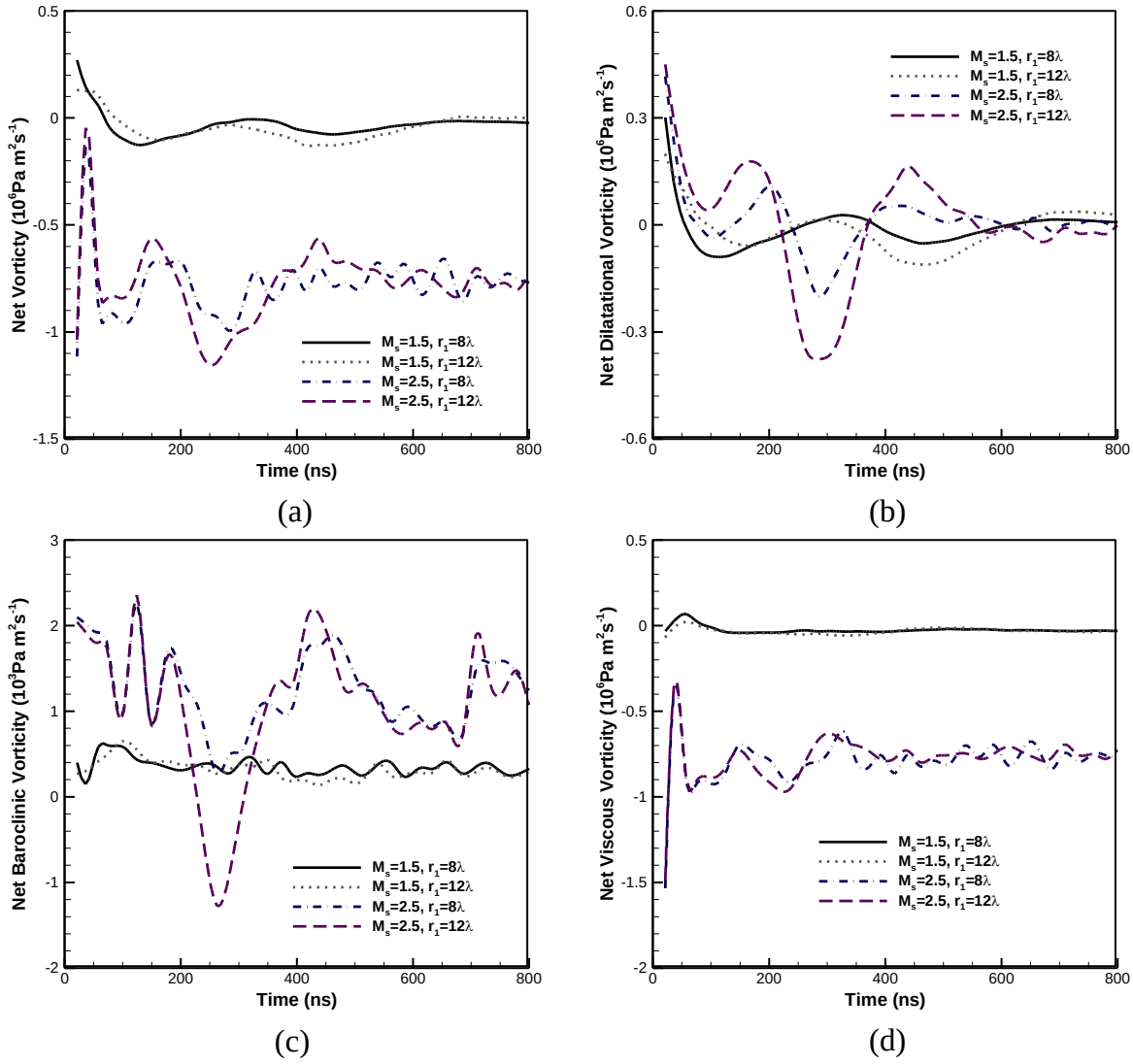

FIG. 18. Vortex deformation in micro SVI: time evolution of (a) net vorticity, (b) net dilatational vorticity, (c) net baroclinic vorticity and, (d) net viscous vorticity with M_v=1.0.

The reason behind this gap may be that the viscous stress dominates the flow structure during the interaction.[40] Strong interaction with a high shock Mach number or a large vortex size causes strong viscous effects and a large dissipation rate, whereas weak interaction with a low shock Mach number or small vortex size yields weak viscous effects and a low dissipation rate. This is one of the major features of the micro SVI in diatomic nitrogen gas, and is also in qualitative agreement with the conclusion for a monatomic gas.[24]

The results of the enstrophy and the dissipation rate show that their evolution dynamics are strongly dependent on the strength of the interactions. Therefore, in order to obtain a better understanding of the physics of the interaction, we conducted a detailed study of the vorticity transportation during the interaction.

Figure 18 illustrates the net vorticity and three components of vorticity transportation for cases 1-4. The results show that the net vorticity and all components reach significant values during the interaction and diminish shortly after passing the vortex. It can be observed that, during the interaction, viscous vorticity generation is the most dominant mechanism, followed by dilatational vorticity and baroclinic vorticity generations. In addition, the viscous effects play a more dominant role in the interaction for strong shock waves (cases 3 and 4), resulting in a significant increase in the dissipation rate, as shown in Fig. 17(b).

3. Effects of interaction parameters on micro SVIs

Interaction parameters—the incident shock Mach number, vortex Mach number, and vortex size—play a critical role in SVI. Therefore, we conducted a detailed investigation of the effects of these interaction parameters on micro SVIs.

a. Effect of incoming shock Mach number

To demonstrate the effects of the incoming shock Mach number in the micro SVIs, three different shock Mach numbers, $M_s = 1.5, 2.5, \text{and } 3.5,$ were selected with the same vortex Mach number $M_v = 1.0,$ and vortex radius $r_1 = 10\lambda$. The sound pressure contours for different incoming shock Mach numbers are depicted in Fig. 19.

It can be observed that the high shock Mach number causes a stronger interaction between the shock and vortex. A strong interaction in the high shock Mach number case tends to deter the diffusion of the expansion wave generated by the vortex. It may be noted that the strength of the compression and rarefaction regions varies with the shock Mach number at the same vortex Mach number and vortex size. Eventually, the high shock Mach number reduces the size of the vortex

region while intensifying the compression and rarefaction regions. Moreover, the high shock Mach number tends to break the siege boundary formed by the vortex, as shown in Figs. 19(b) and 19(c).

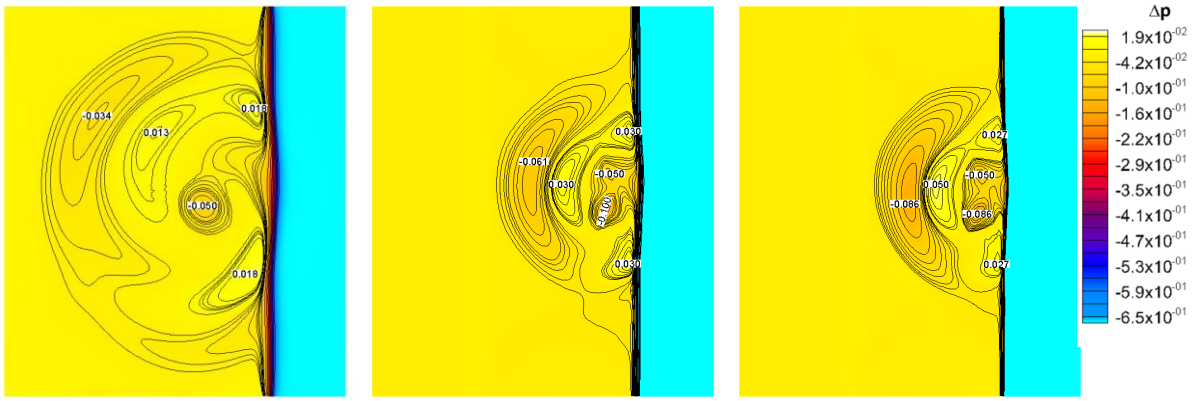

(a) M_s=1.5 (b) M_s=2.5 (c) M_s=3.5

FIG. 19. Effect of incoming shock Mach number in micro SVI: sound pressure contours with $M_v = 1.0$, $r_1 = 10\lambda$.

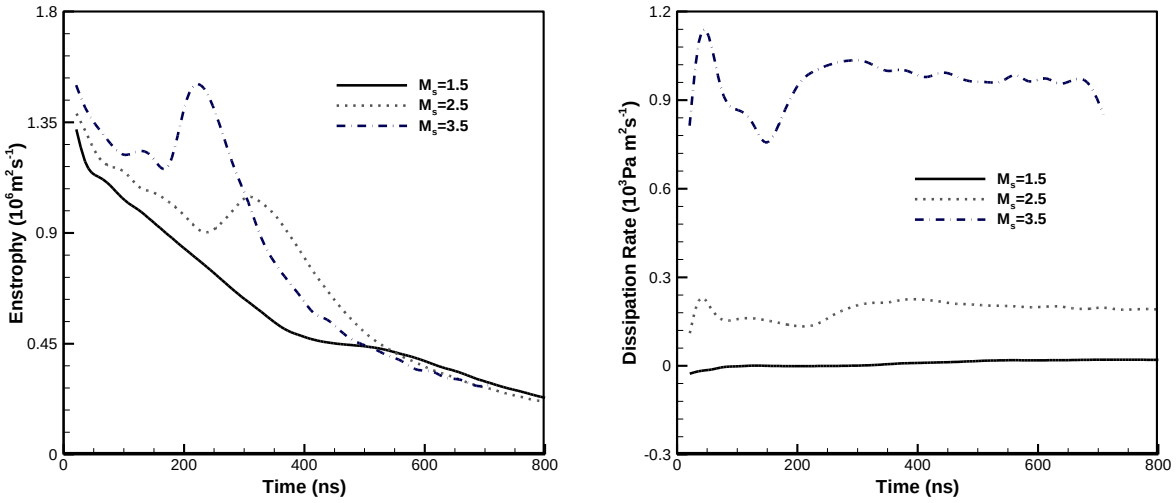

(a) (b)

FIG. 20. Effect of incoming shock Mach number in micro SVI: time evolution of (a) enstrophy and, (b) dissipation rate with $M_v = 1.0$, $r_1 = 10\lambda$.

The effects of incoming shock waves can be further examined through the evolution dynamics of the enstrophy and dissipation rate, which show qualitatively different trends for different shock Mach numbers, as shown in Fig. 20. The results show that an enstrophy increase was observed during interactions for high shock wave cases $M_s = 3.5$ and $M_s = 2.5$, whereas an enstrophy decrease was observed for the low shock wave case $M_s = 1.5$.

Furthermore, with increasing shock Mach number, the increase in the dissipation rate during interaction is enhanced. For example, the increase in the dissipation rate was 1100 Pa m^2/s for $M_s = 3.5,$ while it was reduced to 250 Pa m^2/s for $M_s = 2.5.$

b. Effect of vortex Mach number

To analyse the effects of the vortex Mach number in micro SVIs, three different vortex Mach numbers, $M_v = 0.6, 0.8, 1.0,$ were selected with the same shock Mach number $M_s = 2.5$ and vortex radius $r_1 = 10\lambda$. It may be observed from Fig. 21 that increasing the vortex Mach number strengthens the shock wave-vortex interaction as well as the expanding vortex. Therefore, interaction with a high vortex Mach number produces stronger compression and rarefaction regions.

These vortex Mach number effects can be further analysed using the time evolution of the enstrophy and dissipation rate, as summarized in Fig. 22. It can be observed that the enstrophy increase is enhanced with increasing vortex Mach number. During the interaction, a considerable increase in enstrophy was observed for higher vortex Mach numbers, while a very small enstrophy increase was observed for low vortex Mach numbers. In addition, with increasing vortex Mach number, the increase in the dissipation rate during the interaction was significantly enhanced. For example, the increase was approximately 190 Pa m^2/s for $M_v = 0.6$, while it increased to a very high 250 Pa m^2/s for $M_v = 1.2$.

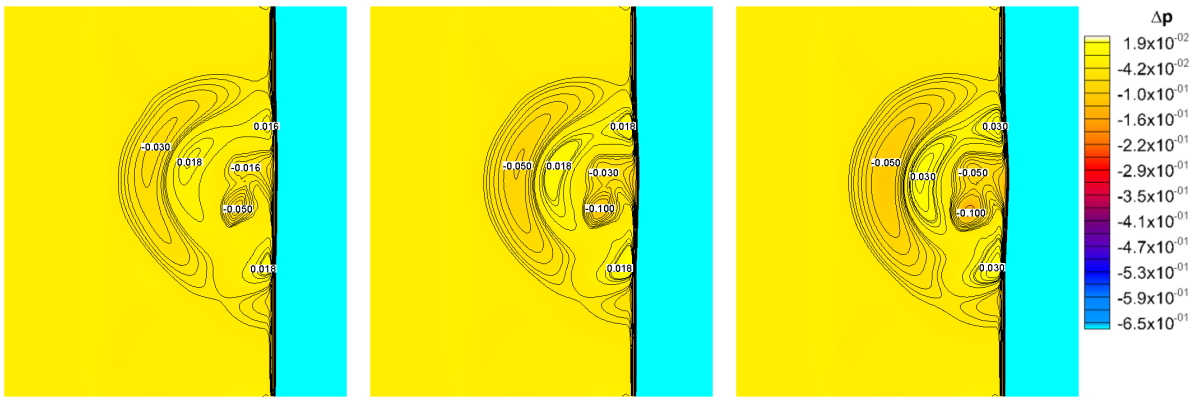

(a) M_v=0.6 (b) M_v=0.8 (c) M_v=1.0

FIG. 21. Effect of vortex Mach number on micro SVI: sound pressure contours with $M_s = 2.5,\ r_1 = 10\lambda.$

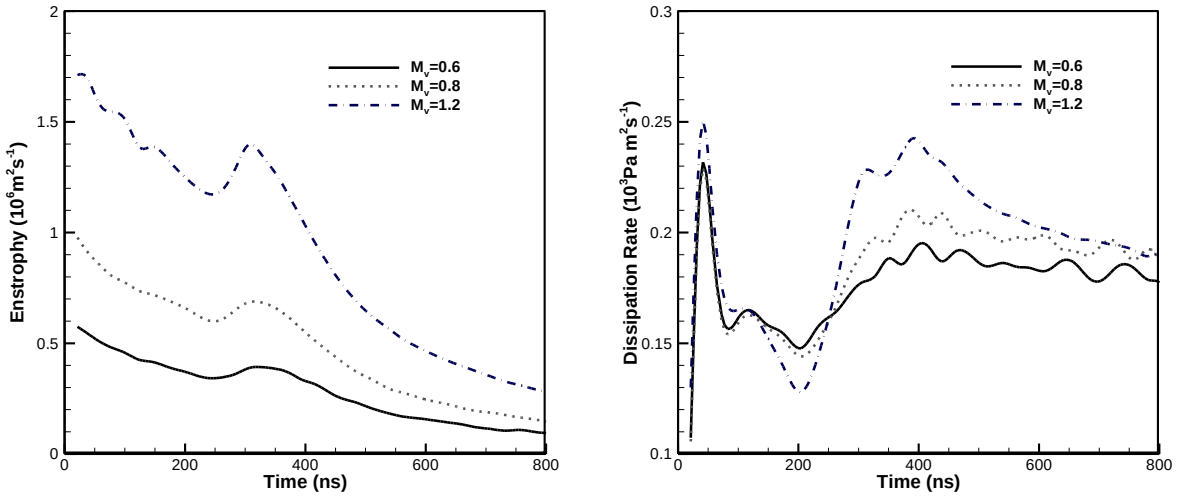

(a) (b)

FIG. 22. Effect of vortex Mach number on micro SVI: time evolution of (a) enstrophy and, (b) dissipation rate with $M_s = 2.5$, $r_1 = 10\lambda$.

c. Effect of vortex size

To investigate the effects of vortex size in micro SVIs, three different cases were selected, $r_1 = 8\lambda, 12\lambda, 16\lambda$, with the same shock Mach number $M_s = 2.5$ and vortex Mach number $M_v = 1.0$. It can be seen in Fig. 23 that, with increasing vortex size, the pressure gradient at the core of the vortex increased significantly, leading to more distinguishable sound pressure contours. In addition, the results confirm that the size of the vortex plays a substantial role in the time evolution of the enstrophy and dissipation rate, as illustrated in Fig. 24. It can be observed that the increase in enstrophy is enhanced with increasing vortex size during the interaction. Therefore, a substantial enstrophy increase was observed in the large vortex ($r_1 = 12\lambda$ and $r_1 = 16\lambda$), while a negligible enstrophy increase was observed in a small vortex ($r_1 = 8\lambda$). Moreover, the increase in the dissipation rate during the interaction was enhanced with increasing vortex size. For example, the increase was found to be 200 Pa m^2/s for $r_1 = 8\lambda$, while it increased to 280 Pa m^2/s for $r_1 = 16\lambda$.

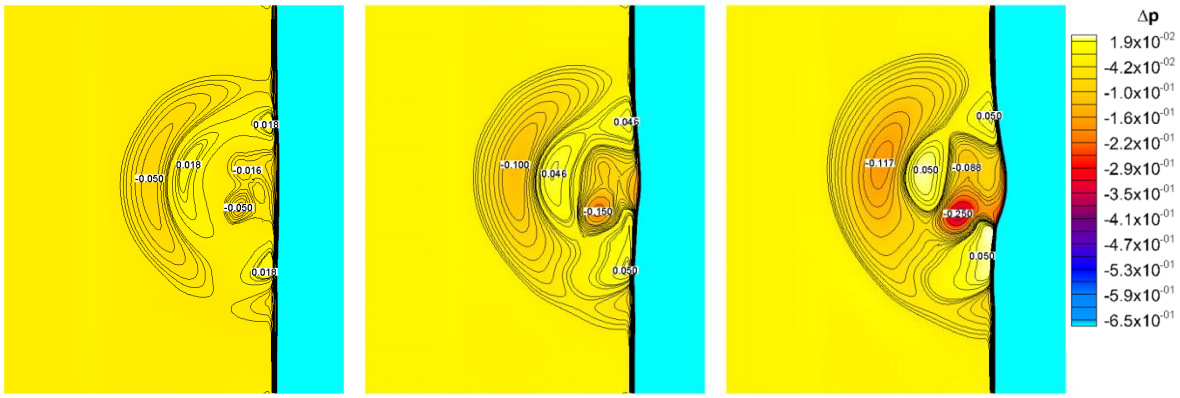

(a) r_1=8λ (b) r_1=12λ (c) r_1=16λ

FIG. 23. Effect of vortex size on micro SVI: sound pressure contours with $M_s = 2.5$, $M_v = 1.0$.

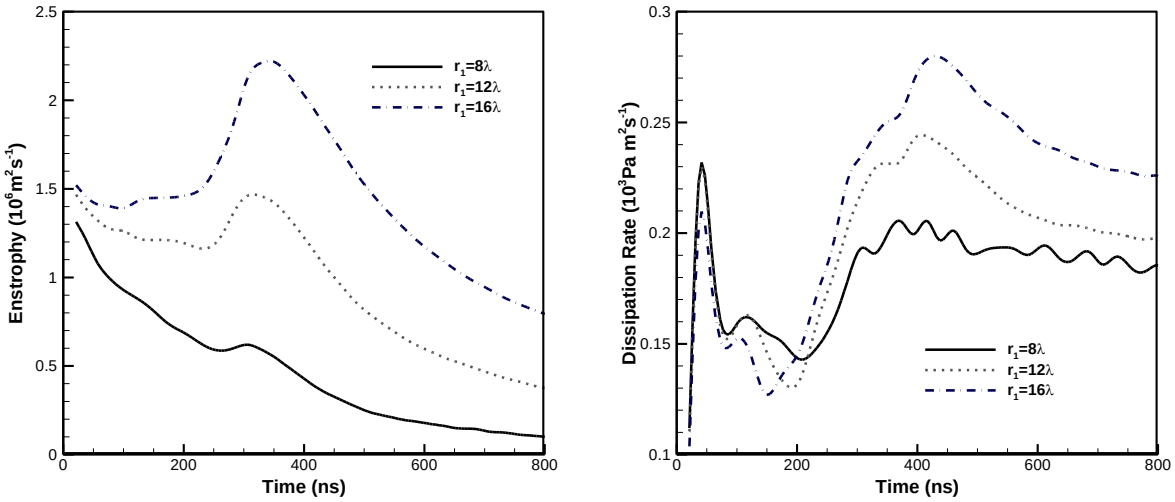

(a) (b)

FIG. 24. Effect of vortex size on micro SVI: time evolution of (a) enstrophy and, (b) dissipation rate with $M_s = 2.5$, $M_v = 1.0$.

4. Comparison of first- and second-order constitutive models in the SVI problem

Figures 25-26 illustrate a comparison between the first- and second-order constitutive models for diatomic (nitrogen) gas in a micro SVI. For this purpose, we selected three different incoming shock Mach numbers: $M_s = 1.5, 2.5, 3.5$ with the same vortex Mach number $M_v = 1.0$ and the vortex radius $r_1 = 10\lambda$. Figure 25 shows that the flow field structures (sound pressure contours) in the first- and second-order constitutive models are non-negligibly different, in particular, for high shock Mach numbers. It may be noted that the second-order constitutive model produces in general stronger

compression and rarefaction regions than the first-order constitutive model. The similar pattern was found in the time evolution of the enstrophy and dissipation rates shown in Fig. 26. It was observed that the time evolution of the enstrophy and dissipation rates in the first- and second-order constitutive models were also considerably different, especially for high shock Mach numbers as shown in Fig. 26. While a notable difference was found in the enstrophy (the second-order constitutive model producing a higher enstrophy), the difference was much more pronounced in the dissipation rate. At a high shock Mach number $M_s = 3.5$, the increase in the dissipation rate was 2600 Pa m^2/s in the first-order constitutive model, while the increase was drastically reduced to 1200 Pa m^2/s in the second-order constitutive model, as shown in Fig. 27(b). At a low shock Mach number $M_s = 1.5$, the increase was found to be 100 Pa m^2/s in the first-order constitutive model, while it became negligible in the second-order constitutive model.

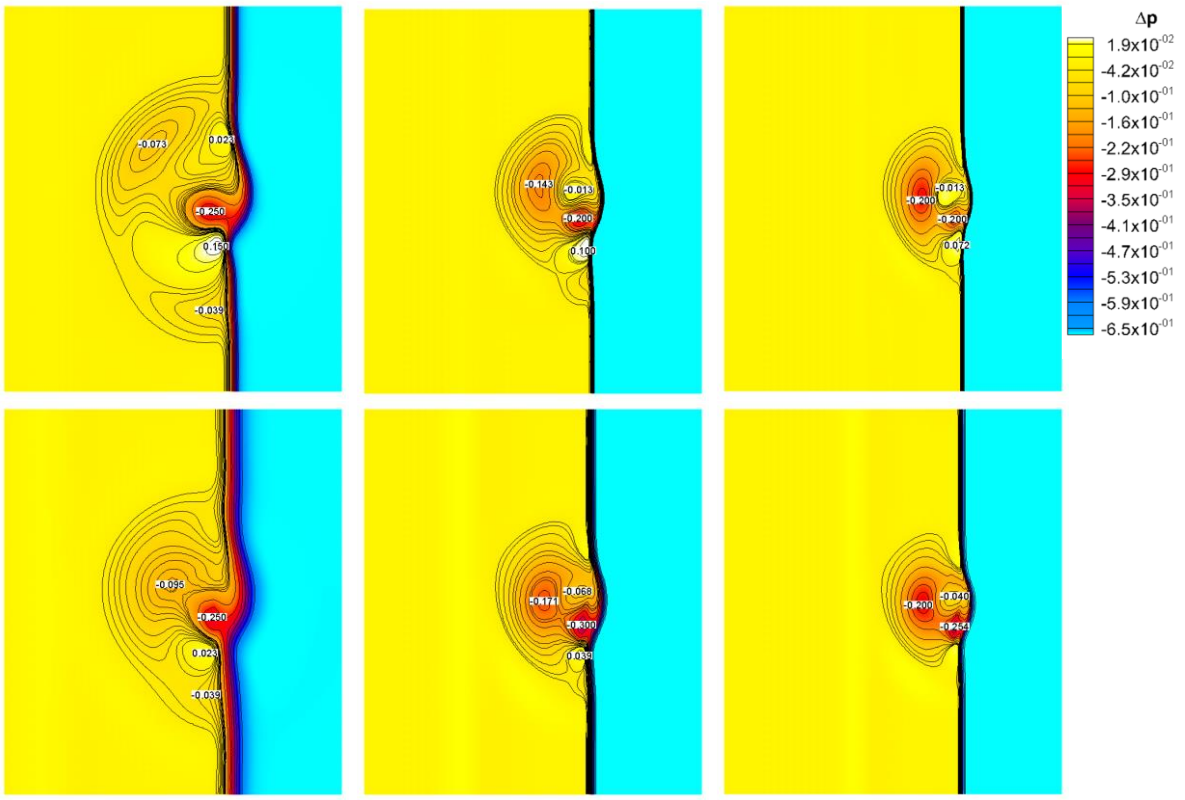

(a) M_s=1.5 (b) M_s=2.5 (c) M_s=3.5

FIG. 25. Comparison of first-order (upper) and second-order (bottom) constitutive models for diatomic (nitrogen) gas on micro SVI: sound pressure contours with different incoming shock Mach number and $M_v = 1.0$, $r_1 = 10\lambda$.

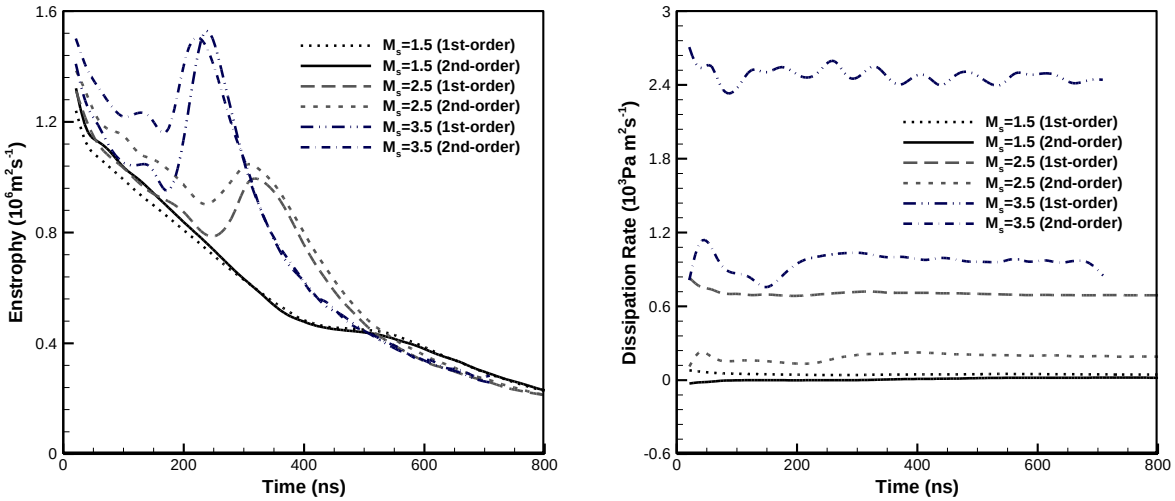

(a) (b)

FIG. 26. Comparison of first-order and second-order constitutive models for diatomic (nitrogen) gas on micro SVI: time evolution of (a) enstrophy and, (b) dissipation rate with $M_v = 1.0$, $r_1 = 10\lambda$.

Figure 27 illustrate a comparison between the first-order constitutive models (standard Navier-Stokes-Fourier and Navier-Fourier without Stokes's hypothesis) and second-order constitutive model for a polyatomic (methane) gas on micro SVI with $M_s = 2.0, M_v = 0.8$, $r_1 = 10\lambda$. It can be observed that the first-order model predicts in general higher degree of thermal non-equilibrium in comparison with the second-order model. It can be also noted that there is a non-negligible difference between the standard Navier-Stokes-Fourier and Navier-Fourier without Stokes's hypothesis models.

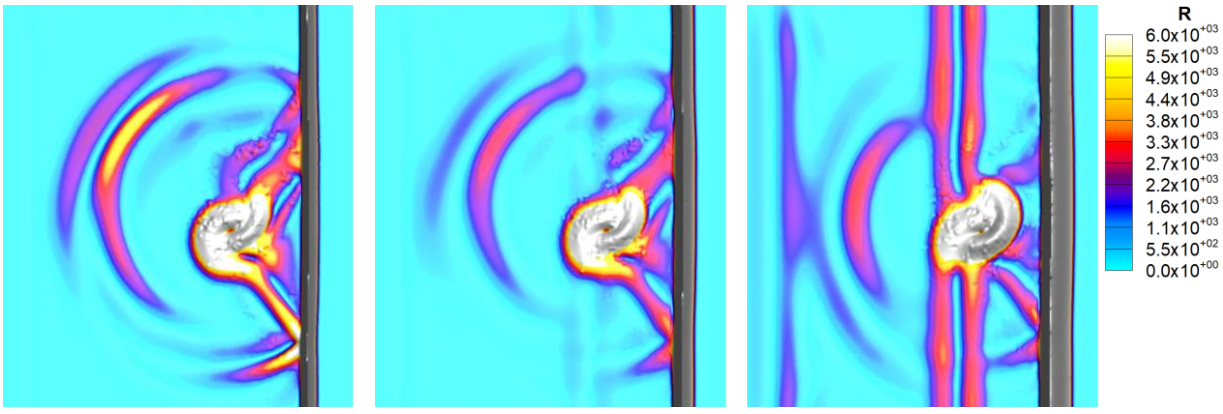

Navier-Stokes-Fourier (f_b=0) Navier-Fourier (f_b=1.33) Second-order model (f_b=1.33)

FIG. 27. Comparison of the classical first-order Navier-Stokes-Fourier, first-order Navier-Fourier and second-order models for polyatomic (methane) gas on micro SVI: degree of non-equilibrium contours with $M_s = 2.0$, $M_v = 0.8, r_1 = 10\lambda$.

5. Summary of characteristics of the micro SVI

The general flow field in a micro SVI, including vortex deformation and the compression and rarefaction regions, is highly dependent of the strength of the incoming shock wave and vortex, and the size of vortex. During the interaction, the viscous vorticity generation was found to be the most dominant factor in the net vorticity transportation process, followed by the generation of dilatational vorticity and baroclinic vorticity.

For strong interactions with a high shock Mach number or large vortex size, a significant increase in the dissipation rate was observed due to the generation of viscous vorticity, resulting in an increase in enstrophy. For weak interactions with low shock Mach number or small vortex size, where the viscous vorticity generation remains negligible, a small increase in the dissipation rate was observed, causing a reduction in enstrophy throughout the interaction process.

The study of the effects of the interaction parameters confirmed that the shock Mach number, the vortex Mach number and the vortex size determine the strength of the interaction and the change in dissipation rate during the interaction. For example, the enstrophy increase or decrease depends on these parameters; it increases with increasing shock and vortex Mach numbers and vortex size. Further, there is a momentary rise in the evolution of enstrophy in such cases.

Finally, the first- and second-order constitutive models yielded a significant difference in the time evolution of enstrophy and dissipation rate in the micro SVI, especially for high shock Mach numbers.

D. Physics of SVPI in diatomic and polyatomic gases

In this subsection, we present the computational results of the shock-vortex pair interaction (SVPI) for diatomic and polyatomic gases. A clockwise-rotating vortex pair parallel to the incident shock wave was considered.

1. Effects of diatomic and polyatomic gases on macro and micro SVPIs

As was done with the SVI, we investigated the effects of diatomic and polyatomic gases on macro and micro SVPIs. We considered two types of SVPI problem: the macro ($M_s = 2.0,\ M_v = 0.8, r_1 = 1000\lambda$) and micro ($M_s = 2.0, M_v = 0.8, r_1 = 10\lambda$) cases. Figure 28 displays the vorticity contours of the macro and micro SVPIs at time t=1000 ns for three different gases. In the

figure, triple points are denoted by (T1, T1’ and T2, T2’); reflected shock waves are denoted by (MR1, MR1’; MR2, MR2’; and MR3, MR3’) and slip lines are denoted by (SL1, SL1’; and SL2, SL2’). Since the vortices are very strong, the coupling effect of the vortex pair becomes significant.

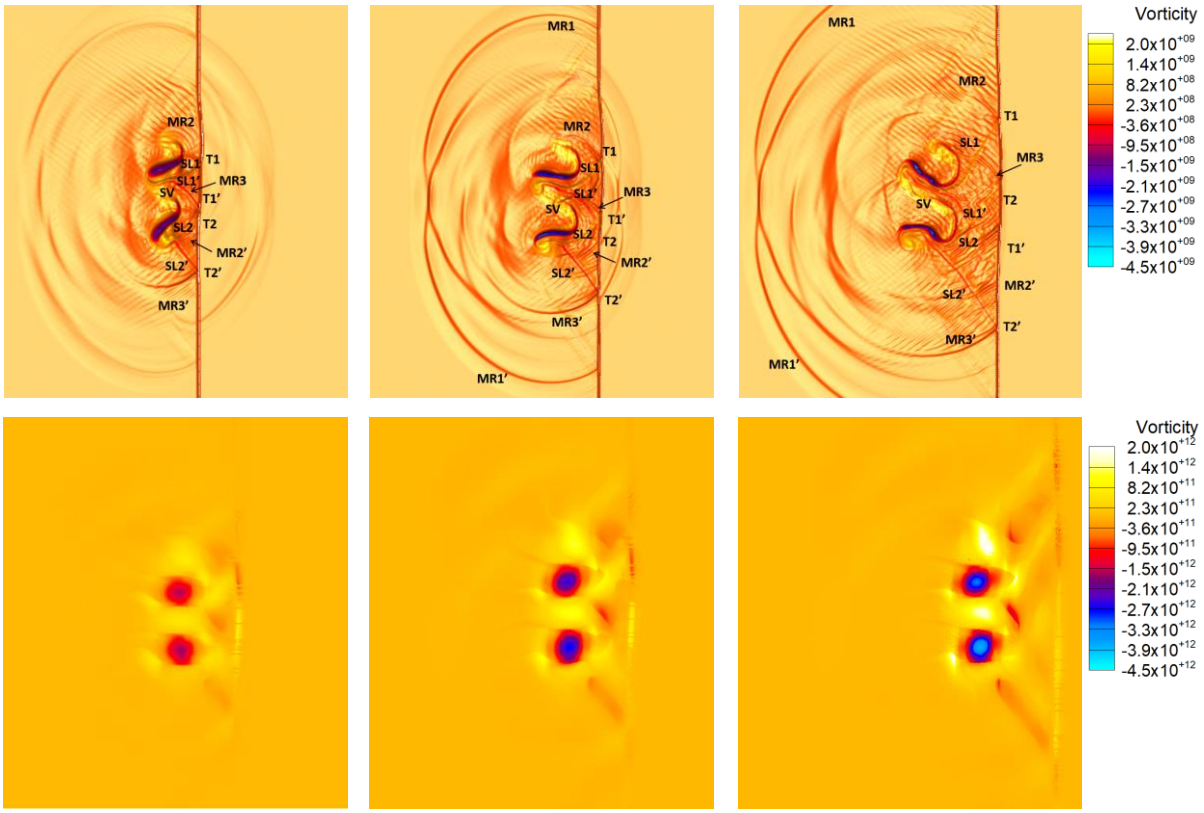

(a) Argon gas, $f_b = 0.0$ (b) Nitrogen gas, $f_b = 0.8$ (c) Methane gas, $f_b = 1.33$

FIG. 28. Effects of diatomic and polyatomic gases on macro SVPI with $M_s = 2.0, M_v = 0.8,$ $r_1 = 1000\lambda$ (top) and micro SVPI with $M_s = 2.0, M_v = 0.8, r_1 = 10\lambda$ (bottom): vorticity contours at $t = 1000\,\text{ns}$.

The evolution of the coupling process results in an interaction-bridge between the vortices (SV). It interacts with the vortex pair before the incident shock waves reaches the vortex pair. It may be noted that the intensity of the interaction-bridge at $f_b = 0$ is very small (see Fig. 28(a)). With increasing f_b value, this intensity increases, as seen in Fig. 28(b) and 28(c). It is also observed that, at $f_b = 0,$ the inner core of the vortex pair with negative vorticity is severely stretched and the outer annular region with positive vorticity begins to detach itself from the inner core (see Fig. 28(a)). This stretching is more pronounced for larger f_b values.

The inner core and the outer annular region are stretched even more for $f_b = 0.8$ (see Fig. 28(b)) and two different structures seem to emerge after interaction at $f_b = 1.33$ (see Fig. 28(c)). On the other hand, the vortex in the micro SVPI remains circular in shape without dramatic stretching in the macro SVPI, and is squeezed in the longitudinal direction, very similar to the micro SVI (compare with Fig. 12).

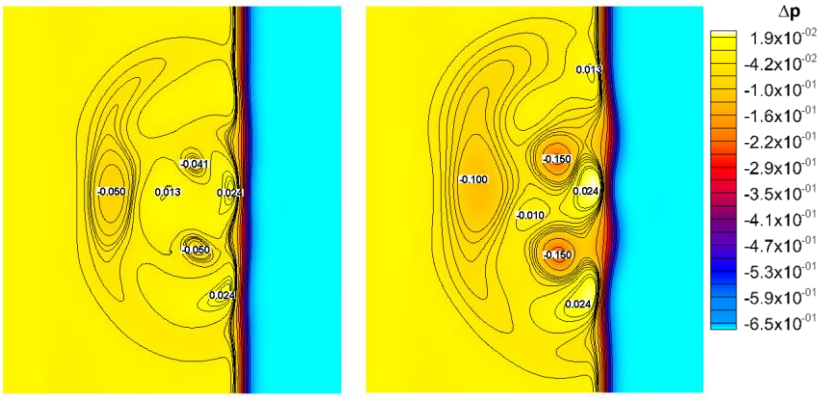

(a) M_s=1.5, $r_1 = 8\lambda$ (b) M_s=1.5, $r_1 = 12\lambda$

(c) M_s=2.5, $r_1 = 8\lambda$ (d) M_s=2.5, $r_1 = 12\lambda$

FIG. 29. Vortex deformation in micro SVPI: sound pressure contours with M_v=1.0.

2. Characteristics of the micro SVPI in diatomic and polyatomic gases

To investigate the flow characteristics of micro SVPIs with regard to the shock strength and vortex size, we considered four cases ($M_s = 1.5$ with $r_1 = 8\lambda$ and 12λ, and $M_s = 2.5$ with $r_1 = 8\lambda$ and 12λ) with the same vortex Mach number $M_v = 1.0$. Again, nitrogen gas was considered as the representative diatomic gas for the study of micro SVPIs.

Figure 29 illustrates four snapshots of sound pressure contours generated by the micro SVPI with different incoming shock Mach numbers and vortex sizes. The results show that the number and strength of the compression and rarefaction regions increases as the Mach number of the incoming shock wave increases. As was observed with the micro SVI, no quadrupolar acoustic wave structure was found for any case of micro SVPI. Moreover, a substantial attenuation of enstrophy in time was found in all cases, as shown in Fig. 30(a). In the $M_s = 1.5$ case, the dissipation rate remained constant over time during the entire interaction, whereas an increase in the dissipation rate was found during active interaction in the $M_s = 2.5$ case, as shown in Fig. 30(b).

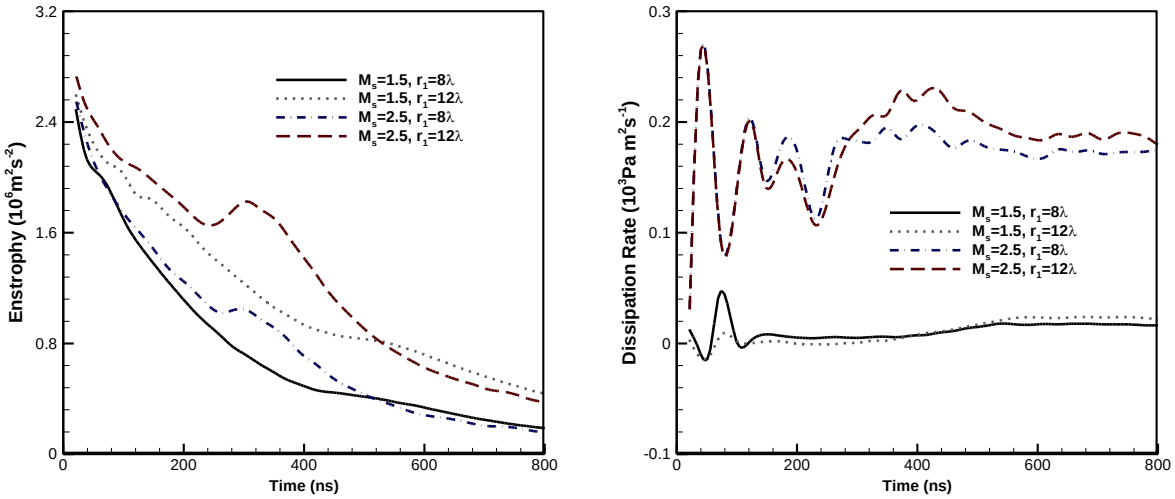

(a) (b)

FIG. 30. Vortex deformation in micro SVPI: time evolution of (a) enstrophy and, (b) dissipation rate with M_v=1.0.

V. CONCLUDING REMARKS

This study focused on an investigation of the non-equilibrium effects in diatomic and polyatomic gases experienced by an initially planar shock wave as it interacts with a single vortex (SVI) or vortex pair (SVPI). For this purpose, the first-order NSF and NF (without the Stokes's hypothesis) and second-order Boltzmann-Curtiss-based constitutive models for diatomic and polyatomic gases were solved in conjunction with the physical conservation laws. The computational models were validated by previous experimental, theoretical and computational results for both macro and micro SVIs.

The results showed that the rotational mode, and in particular, the bulk viscosity, play a critical role in diatomic and polyatomic gases away from equilibrium. The non-equilibrium effects resulted in a substantial change in flow fields in both the macro and micro SVIs.

In particular, some interesting physical features were observed in the diatomic and polyatomic gases; for example, the generation of a third sound wave and additional reflected shock waves with strong and large expansion. The dominance of generated viscous vorticity and a significant increase in enstrophy with increasing bulk viscosity was also observed in the diatomic and polyatomic gases.

Further, a detailed comparative study of macro and micro SVIs was conducted for sound pressure, vorticity and degree of non-equilibrium, the evolution of enstrophy and dissipation rate, and vorticity generation. The computational results showed that the macro and micro SVIs have distinct flow field features and sound generation mechanisms. It is interesting to note that the quadrupolar acoustic wave structure, which was typical in the macro SVI, is no longer observed in any case of micro SVI. Also, while vorticity and degree of non-equilibrium can both describe essential features in the macro SVI, the non-equilibrium parameter was found to be much more effective than vorticity in the micro SVI.

The physics of the micro SVI in diatomic and polyatomic gases was studied primarily through the vortex deformation and evolution dynamics in enstrophy and dissipation rate over an incident shock wave. The results revealed that the general flow field in a micro SVI is highly dependent on the strength of the incoming shock wave and vortex, and the size of the vortex. It was also observed that, during the interaction, the generation of viscous vorticity—particularly in the diatomic and polyatomic gases—remains the most dominant factor in the net vorticity transportation process, followed by the generation of dilatational vorticity and baroclinic vorticity. In addition, it was found that the first- and second-order constitutive models yielded a significant difference in the time evolution of the enstrophy and dissipation rates in the micro SVI, especially for high shock Mach numbers.

The main goal of the present study was to investigate the interaction of two important non-equilibrium phenomena in diatomic and polyatomic gases―the compression dominated shock wave and the velocity-shear dominated vortex―using the fundamental microscopic Boltzmann-Curtiss kinetic theory. Since a similar problem arises in turbulent flows interacting with shock waves, the

current methodology based on the high-order discontinuous Galerkin method may be extended to the computational simulation of shock-turbulence interactions in future investigations.

ACKNOWLEDGEMENTS

This work was supported by the National Research Foundation of Korea funded by the Ministry of Education, Science and Technology (NRF 2015-M1A3A3A02010621 & 2017-R1A2B2007634), South Korea.

REFERENCES

[1]G. G. Stokes, "On the theories of the internal friction of fluids in motion, and of the equilibrium and motion of elastic fluids," Trans. Cambridge Phil. Soc. **8**, 287-305 (1845).

[2]Y. Zhu, C. Zhang, X. Chen, H. Yuan, J. Wu, S. Chen, C. Lee, and M. Gad-el-Hak, "Transition in hypersonic boundary layers: Role of dilatational waves," AIAA J. **54**, 3039 (2016).

[3]R. E. Graves, and B. M. Argrow, "Bulk viscosity: past to present," J. Thermophys. Heat Transfer **13**, 337-342 (1999).

[4]G. Emanuel, "Bulk viscosity of a dilute polyatomic gas," Phys. Fluids A: Fluid Dyn. **2**, 2252-2254 (1990).

[5]G. Emanuel, "Bulk viscosity in the Navier–Stokes equations," Int. J. Eng. Sc. **36**, 1313 (1998).

[6]N. Carlevaro, and G. Montani, "Bulk viscosity effects on the early Universe stability," Mod. Phys. Lett. A **20**, 1729 (2005).

[7]J. F. Brady, A. S. Khair, and M. Swaroop, "On the bulk viscosity of suspensions," J. Fluid Mech. **554**, 109 (2006).

[8]M. Smart, I. Kalkhoran, and S. Popovic, "Some aspects of streamwise vortex behavior during oblique shock wave/vortex interaction," Shock Waves **8**, 243 (1998).

[9]K. R. Meadows, A. Kumar, and M. Hussaini, "Computational study on the interaction between a vortex and a shock wave," AIAA J. **29**, 174 (1991).

[10]S. Pao, and J. Seiner, "Shock-associated noise in supersonic jets," AIAA J. **21**, 687 (1983).

[11]P. Lu, and K. Wu, "On the shock enhancement of confined supersonic mixing flows," Phys. Fluids A: Fluid Dyn. **3**, 3046 (1991).

[12]M.A. Hollingsworth, and E. Richards, "A schlieren study of the interaction between a vortex and a shock wave in a shock tube," Aeronautical Research Council Technical Report No. 17985, FM 2323 (1955).

[13]D. S. Dosanjh, and T. M. Weeks, "Interaction of a starting vortex as well as a vortex street with a traveling shock wave," AIAA J. **3**, 216 (1965).

[14]H. S. Ribner, "Cylindrical sound wave generated by shock-vortex interaction," AIAA J. **23**, 1708 (1985).

[15]J. L. Ellzey, M. R. Henneke, J. M. Picone, and E. S. Oran, "The interaction of a shock with a vortex: shock distortion and the production of acoustic waves," Phys. Fluids **7**, 172 (1995).

[16]O. Inoue, and Y. Hattori, "Sound generation by shock–vortex interactions," J. Fluid Mech. **380**, 81 (1999).

[17]F. Grasso, and S. Pirozzoli, "Shock-wave–vortex interactions: shock and vortex deformations, and sound production," Theor. Comput. Fluid Dyn. **13**, 421 (2000).

[18]S. Zhang, Y. T. Zhang, and C. W. Shu, "Multistage interaction of a shock wave and a strong vortex," Phys. Fluids **17**, 116101 (2005).

[19]A. Chatterjee, and S. Vijayaraj, "Multiple sound generation in interaction of shock wave with strong vortex," AIAA J. **46**, 2558 (2008).

[20]S. Pirozzoli, F. Grasso, and A. D'Andrea, "Interaction of a shock wave with two counter-rotating vortices: Shock dynamics and sound production," Phys. Fluids **13**, 3460 (2001).

[21]O. Inoue, T. Takahashi, and N. Hatakeyama, "Separation of reflected shock waves due to the secondary interaction with vortices: Another mechanism of sound generation," Phys. Fluids **14**, 3733 (2002).

[22]S. Zhang, S. Jiang, Y. T. Zhang, and C. W. Shu, "The mechanism of sound generation in the interaction between a shock wave and two counter-rotating vortices," Phys. Fluids **21**, 076101 (2009).

[23]K. Koffi, Y. Andreopoulos, and C. B. Watkins, "Dynamics of microscale shock/vortex interaction," Phys. Fluids **20**, 126102 (2008).

[24]H. Xiao, and R. S. Myong, "Computational simulations of microscale shock–vortex interaction using a mixed discontinuous Galerkin method," Comput. Fluids **105**, 179 (2014).

[25]R. S. Myong, "A generalized hydrodynamic computational model for rarefied and microscale diatomic gas flows," J. Comput. Phys. **195**, 655 (2004).

[26]R. S. Myong, "On the high Mach number shock structure singularity caused by overreach of Maxwellian molecules," Phys. Fluids **26**, 056102 (2014).

[27]B. C. Eu, and Y. G. Ohr, "Generalized hydrodynamics, bulk viscosity, and sound wave absorption and dispersion in dilute rigid molecular gases," Phys. Fluids **13**, 744 (2001).

[28]B. C. Eu, Kinetic Theory and Irreversible Thermodynamics (Wiley, 1992).

[29]C. Curtiss, "The classical Boltzmann equation of a gas of diatomic molecules," J. Chem. Phys. **75**, 376 (1981).

[30]R. S. Myong, "A full analytical solution for the force-driven compressible Poiseuille gas flow based on a nonlinear coupled constitutive relation," Phys. Fluids **23**, 012002 (2011).

[31]A. Rault, G. Chiavassa, and R. Donat, "Shock-vortex interactions at high Mach numbers," J. Sci. Comput. **19**, 347 (2003).

[32] G. Bird, Molecular Gas Dynamics and the Direct Simulation of Gas Flows (Clarendon, Oxford, 1994).

[33]M. S. Cramer, "Numerical estimates for the bulk viscosity of ideal gases," Phys. Fluids **24**, 066102 (2012).

[34]S. Chapman, and T. G. Cowling, The Mathematical Theory of Non-uniform Gases (Cambridge University Press, Cambridge, 1970).

[35]R. S. Myong, "Thermodynamically consistent hydrodynamic computational models for high-Knudsen-number gas flows," Phys. Fluids **11**, 2788 (1999).

[36]N. T. Le, H. Xiao, and R. S. Myong, "A triangular discontinuous Galerkin method for non-Newtonian implicit constitutive models of rarefied and microscale gases," J. Comput. Phys. **273**, 160 (2014).

[37]F. Bassi, and S. Rebay, "A high-order accurate discontinuous finite element method for the numerical solution of the compressible Navier–Stokes equations," J. Comput. Phys. **131**, 267 (1997).

[38]B. Cockburn, and C. W. Shu, "The Runge–Kutta discontinuous Galerkin method for conservation laws V: multidimensional systems," J. Comput. Phys. **141**, 199 (1998).

[39]D. Dosanjh, and T. Weeks, "Sound generation by shock-vortex interaction," AIAA J. **5**, 660 (1967).

[40] Y. Andreopoulos, J. H. Agui, and G. Briassulis, "Shock wave turbulence interactions," Annu. Rev. Fluid Mech. **32**, 309 (2000).